공학박사 학위논문

Predictive dynamic substructuring using theoretical transfer characteristics of subsystem

서브시스템의 이론적 전달특성을 이용한 예측적 동특성 합성기법

2023 년 8 월

서울대학교 대학원

기계항공공학부

박 한 솔

Predictive dynamic substructuring using theoretical transfer characteristics of subsystem

서브시스템의 이론적 전달특성을 이용한
예측적 동특성 합성기법

지도교수 강 연 준

이 논문을 공학박사 학위논문으로 제출함
2023 년 4 월

서울대학교 대학원
기계항공공학부
박 한 솔

박한솔의 공학박사 학위논문을 인준함
2023 년 6 월

위 원 장 _____

부위원장 _____

위 원 _____

위 원 _____

위 원 _____

ABSTRACT

Predictive dynamic substructuring using theoretical transfer characteristics of subsystem

Hansol Park

School of Mechanical and Aerospace Engineering

The Graduate School

Seoul National University

This study proposes a method for predicting changes in the transfer characteristics of a combined system according to the modification of a frame-shaped subcomponent without additional experiment. To predict the dynamic characteristics of a combined system, the dynamic behaviors of a frame-shaped substructure were theoretically analyzed using a simplified formulation. Based on the Euler–Bernoulli and Timoshenko–Ehrenfest beam theories, analytic solutions of dynamic behaviors are defined according to the boundary conditions at the end of each beam component and coupling constraints at the structural joint of the system. The entire set of equations are arranged as a linear algebraic formulation, and it has large scalability of the shape of the frame-shaped

subcomponent. The motions are defined by the coefficient vector computed from the characteristic matrix and the external force vector. The analyzed dynamic characteristics of the modified subcomponent are combined with the measured dynamic properties of the other subsystem using the dynamic substructuring technique. To use this component coupling method, the concepts of joint property are introduced and applied to combining the predicted dynamic characteristics of the frame-shaped substructure and the measured characteristics of the rest of the target system. This dynamic substructuring process is experimentally verified by testing a vehicle system. One of the frame-shaped parts of the vehicle suspension system is altered to a rigid frame structure, and the transfer characteristics of the full vehicle system are predicted by the proposed predictive dynamic substructuring technique. The prediction showed high agreement with the measured transfer function, confirming the accuracy of the prediction. In addition, two cases of applications are introduced in this study to utilize the proposed method. One is the prediction of dynamic responses of the vehicle system. Predicted transfer characteristics of the combined system are multiplied with the vitual input force, called blocked force, so that the changes in noise and vibration which are transmitted to the passenger are calculated without

additional experiment. The other application is the prediction of perceptual characteristics for the vibration transmitted to the human body. A quantification model of subjective feeling about the vehicle induced vibration is developed under the name of ride quality index. The relationship between subjectively evaluated scores of ride quality and measured vibration that is transmitted to the human body is statistically investigated to evaluate the vehicle ride quality. Multiple linear regression analysis and principal component analysis are performed to simplify the testing process and formulate the ride quality index models. The reliability of the constructed models is confirmed according to computed statistical indicators and an additional verification procedure. Through this series of studies, it is possible to predict the change in the transfer characteristics of complete vehicle system for the modification of a specific subcomponent without additional experiments, and even to predict the change in dynamic responses and ride quality perceived by the driver.

Keywords: Transfer characteristics, Beam vibration theory,

Dynamic subtructuring, Rigid frame structure, Ride quality

Student Number: 2015-20728

TABLE OF CONTENTS

LIST OF TABLES

LIST OF FIGURES

CHAPTER 1

INTRODUCTION

The automobile industry has made enormous strides over the past century since the first vehicles were mass-produced. With an increased demand for premium automobiles, ergonomic concerns including noise, vibration and harshness (NVH) issues have received significant study interest after the early technical progress concentrated on driving performance and fuel efficiency. In order to solve the NVH problem, an evaluation procedure that quantitatively evaluates the level of noise and vibration induced by the vehicle is required. So far, several studies for evaluations of NVH levels have evolved the technology for experimental measurement and analysis of vibration with an in-depth understanding of the vibration generation mechanism. Nevertheless, the proactive assessment method remains a problem to be solved. Complex machinery system such as a vehicle is composed of various parts, and that makes predictive approaches inaccurate. Therefore, at the present time, analysis and evaluation of vehicle induced vibration can only be performed experimentally with an actual prototype.

In an attempt to simplify the evaluation of the dynamic behaviors of complex system, the vibration transfer characteristics of a vehicle system are

estimated by using the dynamic substructuring technique. The dynamic substructuring was studied by Tsai and Chou [1] estimating the dynamic responses of steel beams with single bolted joint, and Jetmundsen et al. [2] introduced the dynamic substructuring method that enhanced the usability and efficiency of dynamic modeling. This method is still mainly used substructuring technique because it is theoretically reasonable and easy to apply to practical problems. This technique is a dynamic estimation of combined structures using the dynamic properties of substructures which obtained by spectral testing. If one of the substructures modified, the dynamic properties of a combined structure can be predicted by testing not the whole combined structure but only the changed part. This makes the evaluation process simple when trying to improve the vibratory characteristics of the entire system by using modifications in specific parts. Furthermore, with the use of dynamic substructuring techniques that depend on frequency response function (FRF) data, numerous research has been done to estimate the dynamic properties of entire systems that have two or more connected substructures. Ewins and Gleeson [3] investigated at how system parameters were applied using FRFs and offered a technique to determine the dynamic characteristics of a structure. Similar to this, a method for determining joint characteristics using partly measured FRFs was proposed by Wang et al. [4]. To estimate joint properties

using FRFs, Mehrpouya et al. [5] suggested an inverse receptance coupling approach. Tol [6] presented a joint parameter updating algorithm and used FRF information to determine the dynamic properties of a bolted joint. In addition, Cao et al. [7] suggested a method for updating finite element models to accurately identify joint properties and a synthesis model was considered as a coupling stiffness matrix by Yang et al. [8], who thus improved a joint identification approach. With the aid of system response data and an inverse substructure method that did not require the information of individual substructures, Zhen et al. [9] estimated the FRFs of a multi-coupling system. Meanwhile, Allen et al. [10] used a modal substructuring technique to minimize the effects of flexible fixtures. In addition, Moorhouse et al. [11] applied a transfer path analysis in an operational condition using a dynamic substructuring method and the blocked force occurring at a joint interface. A hybrid dynamic model was presented by Klaassen et al. [12] utilizing the system equivalent model mixing technique. When using the dynamic substructuring technique in automotive domains, there are still practical limits despite the several studies on model improvement. In addition to reviewing dynamic substructuring and conducting practical research employing the substructuring technique by Van der Seijs et al. [13], They predicted the dynamic characteristics of a completed automotive steering column system [14].

With an understanding of the constraints of practical testing, Kang [15,16] and Song et al. [17] introduced a test jig to construct a vehicle suspension system using a dynamic substructuring technique. The dynamic substructuring method was suggested as having useful applications by Kim et al. [18] who assessed system characteristics using virtual parameters. In this study, accuracy improved method [19] of dynamic substructuring was used to precisely calculated the dynamic properties by introducing the concept of virtual point transform.

However, no matter how accurate the estimation of this method is, it is an experimental method based on measured FRF data, so a practical test sample is required. To overcome this limitation, the vibratory response of a rigid frame subsystem is analyzed based on the beam vibration theories with the material and geometric information of beam-shaped parts. Several techniques have been studied to predict the dynamic behavior of rigid frame structures. For example, Chang [20] provided an analytic solution for the vibrations of a frame structure, which is a coupled structure of two or three beam components. In this study, the overall formulation was a series of equations consisting of equations from the supported boundary condition, which was derived based on physical constraints. Kirk and Wiedemann [21] theoretically analyzed and formulated a complete series equation of a beam with large masses at each end, and the

vibration problem of a planar frame structure was solved using a hybrid analytical and numerical method proposed by Lin and Ro [22]. Williams [23] applied an advanced algorithm to analyze the natural frequencies of cyclically symmetric structures. The algorithm was extended based on the stiffness matrix method and was used to calculate the eigenvalue of the structural model composed of rotationally repeated beam components. For a more complicated frame structure, the transfer dynamic stiffness coefficient method was proposed by Moon and Choi, which considers each beam component of the frame structure as a distributed mass component [24]. In addition to these theoretical analyses, different approaches have been adopted to analyze the dynamic behavior of a combined beam structure. Chouvion et al. [25] used a wave propagation approach to predict the dynamics in a ring beam structure, and Mei [26] applied a similar method for a rectangular frame. Ritto et al. [27] used the Bayesian approach to evaluate the behavior of a beam coupled with a wall under varying joint stiffnesses. In addition to these theoretical analyses, test-based estimations have also been performed for practical applications. A synthesis method for the dynamic properties of system components was proposed by Tsai and Chou using the dynamic properties of a structural joint, which is obtained as a frequency response function (FRF) [28]. Starting from this research, the FRF-based substructuring method was refined to estimate the coupled system

using experimental data of the subcomponents [29]. Based on this predictive method, the blocked force [30] and virtual point transformation technique [31] was suggested to improve the estimation accuracy, and the concept of a virtual spring was introduced to simplify the test procedure [32]. These practical methods have improved the usability of substructuring estimation in the industrial field. Nevertheless, experimental data from subcomponents are still required to evaluate the dynamic characteristics of the coupled structure, limiting the predictive use of these methods. In addition, the above-mentioned theoretical studies are useful for estimating the system responses; however, the prediction is limited to the model included in the study, and different formulations need to be applied for different models and conditions, which results in low versatility.

This study aims to provide a simplified and versatile formulation for theoretically predicting the dynamic behavior of a rigid frame structure. The dynamic properties of the beam structure with an arbitrarily coupled angle are analyzed based on two well-known beam vibration theories: the Euler–Bernoulli and Timoshenko–Ehrenfest beam theories. The characteristic equations were derived from the boundary conditions at both ends of the beam components and the equation of motion of the structural joint. The vibration mode conversion between the coupled components was considered according

to the compatibility and force equilibrium conditions at the joint. Furthermore, the derived characteristic equations were organized in the form of a matrix formula where constant matrixes of material properties of each sub-component, basis matrixes of differential equation, and coefficient vectors were linearly combined. This matrix form of characteristic equation was applied to all joints and boundaries of the structure and was arranged in a single linear algebraic expression. With this formulation, the computation of analytic solution is quite simple because only a simple inverse matrix calculation is required instead of solving large series of partial differential equation. The dynamic properties of rigid frame structure were analytically defined and verified through a comparison of the modal parameters with the calculated and test results. Using this linear algebraic formulation, the estimation of the three-dimensional dynamic behaviors of the rigid frame structure improved its computational efficiency and model scalability. With this procedure, frequency response of the frame-shaped subsystem is easily analyzed and applicable on the dynamic substructuring technique. Thus, changes of the transfer characteristics of entire combined system are predicted without additional experiment according to the change of design parameters of the subsystem.

In this study, two application examples are included for utilization of the proposed predictive method. Dynamic responses at the human contact point of

the vehicle system are predicted using predictive dynamic substructuring. Assuming the blocked force, which is equivalent input force that does not change regardless of the change of the passive subsystem, the vibratory responses of vehicle system can be predicted. Furthermore, this study includes the quantitative evaluation of perceptual characteristics for vehicle induced vibration which is challenging to quantify. For this application case, an experimental method to evaluate the vehicle ride quality is introduced. This robust method assesses the ride quality score of the vehicle with the measured vibration, as opposed to the conventional method which relies on the unstable impressions of a small number of evaluators. Also, the evaluation of ride quality in this research is carried out independently for two types of vibration that have different vibratory characteristics and lead to different sensations of the human body. In order to develop the ride quality index (RQI) models, objective measurements and subjective evaluations were both performed at the same time. To simplify the test procedure and develop the RQI models, principal component analysis and multiple linear regression analysis were used, respectively. The computation of statistical indicators was conducted to ensure the reliability of the designed RQI models, and an additional verification process was carried out to verify their accuracy. By applying the predictive dynamic substructuring to the developed RQI models, the change of vehicle

ride quality can be predictively and evaluated quantitatively according to the design change of subsystem.

The remainder of this study is organized as follows. In chapter 2, the theories and the basic formulations to predict vibration of combined systems are briefly introduced. Chapter 3 includes the method for analysis of a frame-shaped substructure. The prediction of transfer characteristics of entire system using computed FRF data of the subsystem is performed with the dynamic substructuring technique in chapter 4. In chapter 5, two application cases are described as mentioned above. Finally, conclusions are discussed in chapter 6.

CHAPTER 2

GENERAL INTRODUCTION FOR DYNAMIC SUBSTRUCTURING

2.1 Introduction

Vibration responses of a complex system are estimated by using dynamic substructuring technique which combining FRF data of subcomponents into transfer characteristics of entire system. In this study, a system is divided into two subsystem that one of the subcomponents is a frame structure and the other is the rest of the whole system. Assuming that the transfer characteristics of the rest of the system except for the frame substructure were given, changes in the dynamic responses of the combined system are predictable by using dynamic substructuring technique which combining the transfer characteristics of divided subsystems. This chapter covers the concepts and the formulations of dynamic substructuring technique essential to adopting this approach. The theoretical background and the underlying assumption for dynamic substructuring are introduced, followed by the formula expansion.

2.2 Dynamic substructuring

The theoretical concept of dynamic substructuring technique was organized by Tsai [1]. The dynamic characteristics FRF are generally used for this method, so it is also called FRF based substructuring (FBS) method. This method is for obtaining the coupled dynamic characteristics of two separated substructure. As shown in Fig. 2.1, substructure A and B are combined at the joint J. Input point I and output point O are both located in subsystem A and the dynamic responses of both points can be expressed as a matrix form with the displacement u, force f, and transfer function H of subsystems.

$$\begin{bmatrix} u_O \\ u_J^{\mathrm{A}} \\ u_J^{\mathrm{B}} \end{bmatrix} = \begin{bmatrix} \mathrm{H}_{O,I}^{\mathrm{A}} & \mathrm{H}_{O,J}^{\mathrm{A}} & 0 \\ \mathrm{H}_{J,I}^{\mathrm{A}} & \mathrm{H}_{J,J}^{\mathrm{A}} & 0 \\ 0 & 0 & \mathrm{H}_{J,J}^{\mathrm{B}} \end{bmatrix} \begin{bmatrix} f_I \\ f_J^{\mathrm{A}} \\ f_J^{\mathrm{B}} \end{bmatrix} \tag{2-1}$$

At this joining point, the force equilibrium and compatibility condition are assumed so that a rigid coupling condition is satisfied. These two coupling condition at the joint are represented as follows:

$$f_J^{\mathrm{A}} + f_J^{\mathrm{B}} = 0, \tag{2-2}$$

$$u_J^{\mathrm{A}} = u_J^{\mathrm{B}}. \tag{2-3}$$

Eq. (2-2) describes the force equilibrium condition which represents the zero net force, and Eq. (2-3) describes the compatibility condition which represents the rigid connection between substructure A and B. Using Eqs. (2-1)–(2-3), the force f_J^{A} that transmitted to substructure A from the joint J and the displacement of output point u_O can be stated as

$$f_J^{\mathrm{A}} = -\left(\mathrm{H}_{J,J}^{\mathrm{A}} + \mathrm{H}_{J,J}^{\mathrm{B}}\right)^{-1}\mathrm{H}_{J,I}^{\mathrm{A}}\mathrm{f}_I \tag{2-4}$$

$$u_O = \left[\mathrm{H}_{O,I}^{\mathrm{A}} - \mathrm{H}_{O,J}^{\mathrm{A}}\left(\mathrm{H}_{J,J}^{\mathrm{A}} + \mathrm{H}_{J,J}^{\mathrm{B}}\right)^{-1}\mathrm{H}_{J,I}^{\mathrm{A}}\right] f_I \tag{2-5}$$

Hence, the transfer function of the combined structure $\mathrm{H}_{O,I}^{\mathrm{AB}}$ can be estimated by transfer characteristics of substructures.

$$\mathrm{H}_{O,I}^{\mathrm{AB}} = \mathrm{H}_{O,I}^{\mathrm{A}} - \mathrm{H}_{O,J}^{\mathrm{A}}\left(\mathrm{H}_{J,J}^{\mathrm{A}} + \mathrm{H}_{J,J}^{\mathrm{B}}\right)^{-1}\mathrm{H}_{J,I}^{\mathrm{A}} \tag{2-6}$$

Eq. (2-6) is the general formulation of dynamic substructuring techniques which can be applied for more complex systems with multiple inputs and multiple joints. Considering the systems with two inputs and two joints depicted in Fig. 2.2, the formulation of dynamic responses in Eq. (2-1) changes to Eq. (2-7).

$$\begin{bmatrix} u_O \\ u_{J_1}^{\mathrm{A}} \\ u_{J_2}^{\mathrm{A}} \\ u_{J_1}^{\mathrm{B}} \\ u_{J_2}^{\mathrm{B}} \end{bmatrix} = \begin{bmatrix} \mathrm{H}_{O,I_1}^{\mathrm{A}} & \mathrm{H}_{O,I_2}^{\mathrm{A}} & \mathrm{H}_{O,J_1}^{\mathrm{A}} & \mathrm{H}_{O,J_2}^{\mathrm{A}} & 0 & 0 \\ \mathrm{H}_{J_1,I_1}^{\mathrm{A}} & \mathrm{H}_{J_1,I_2}^{\mathrm{A}} & \mathrm{H}_{J_1,J_1}^{\mathrm{A}} & \mathrm{H}_{J_1,J_2}^{\mathrm{A}} & 0 & 0 \\ \mathrm{H}_{J_2,I_1}^{\mathrm{A}} & \mathrm{H}_{J_2,I_2}^{\mathrm{A}} & \mathrm{H}_{J_2,J_1}^{\mathrm{A}} & \mathrm{H}_{J_2,J_2}^{\mathrm{A}} & 0 & 0 \\ 0 & 0 & 0 & 0 & \mathrm{H}_{J_1,J_1}^{\mathrm{B}} & \mathrm{H}_{J_1,J_2}^{\mathrm{B}} \\ 0 & 0 & 0 & 0 & \mathrm{H}_{J_2,J_1}^{\mathrm{B}} & \mathrm{H}_{J_2,J_2}^{\mathrm{B}} \end{bmatrix} \begin{bmatrix} f_{I_1} \\ f_{I_2} \\ f_{J_1}^{\mathrm{A}} \\ f_{J_2}^{\mathrm{A}} \\ f_{J_1}^{\mathrm{B}} \\ f_{J_2}^{\mathrm{B}} \end{bmatrix} \tag{2-7}$$

The responses, input forces and the transfer functions are tied as a form of vector or matrix for each input and joint as Eq. (2-8)–(2-11).

$$\mathbf{u}_{\boldsymbol{J}} = \begin{bmatrix} u_{J_1} \\ \vdots \\ u_{J_2} \end{bmatrix} \tag{2-8}$$

$$\mathbf{f}_{\boldsymbol{I}} = \begin{bmatrix} f_{I_1} \\ \vdots \\ f_{I_2} \end{bmatrix}, \ \mathbf{f}_{\boldsymbol{J}} = \begin{bmatrix} f_{J_1} \\ \vdots \\ f_{J_2} \end{bmatrix} \tag{2-9}$$

$$\mathbf{H}_{\boldsymbol{p},\boldsymbol{q}} = \begin{bmatrix} \mathrm{H}_{p_1,q_1} & \cdots & \mathrm{H}_{p_1,q_m} \\ \vdots & \ddots & \vdots \\ \mathrm{H}_{p_n,q_1} & \cdots & \mathrm{H}_{p_n,q_m} \end{bmatrix} \tag{2-10}$$

Using this form, the dynamic responses formulation of the complex system with two inputs and two joints are turned into the identical equation in Eq. (2-1).

$$\begin{bmatrix} \mathbf{u}_{\boldsymbol{O}} \\ \mathbf{u}_{\boldsymbol{J}}^{\mathbf{A}} \\ \mathbf{u}_{\boldsymbol{J}}^{\mathbf{B}} \end{bmatrix} = \begin{bmatrix} \mathbf{H}_{\boldsymbol{O},\boldsymbol{I}}^{\mathbf{A}} & \mathbf{H}_{\boldsymbol{O},\boldsymbol{J}}^{\mathbf{A}} & \mathbf{0} \\ \mathbf{H}_{\boldsymbol{J},\boldsymbol{I}}^{\mathbf{A}} & \mathbf{H}_{\boldsymbol{J},\boldsymbol{J}}^{\mathbf{A}} & \mathbf{0} \\ \mathbf{0} & \mathbf{0} & \mathbf{H}_{\boldsymbol{J},\boldsymbol{J}}^{\mathbf{B}} \end{bmatrix} \begin{bmatrix} \mathbf{f}_{\boldsymbol{I}} \\ \mathbf{f}_{\boldsymbol{J}}^{\mathbf{A}} \\ \mathbf{f}_{\boldsymbol{J}}^{\mathbf{B}} \end{bmatrix} \tag{2-6}$$

Therefore, the formulation of dynamic substructuring in Eq. (2-6) can be applied to multi-input and multi-joint system. Based on the relationship in Eq. (2-6), the transfer function of an entire structure can be estimated for the change of the transfer function of a subsystem B. In this study, the transfer characteristics of the combined system vary according to the material and geometric changes of the rigid frame substructure B, and it is predicted using this dynamic substructuring technique.

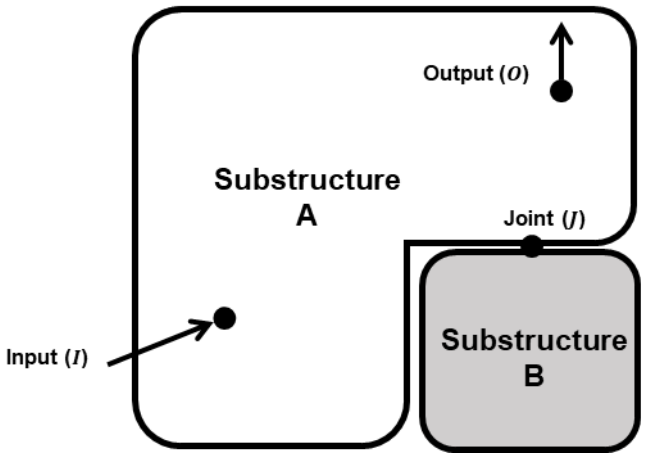

Figure 2.1 Configuration for a structure with substructures A and B combined at the joining point J.

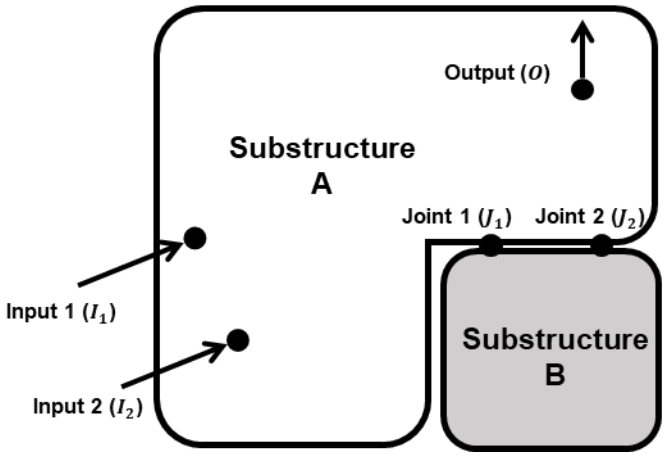

Figure 2.2 Configuration for a structure with multi-input and multi-joint.

CHAPTER 3

PREDICTION OF DYNAMIC CHARACTERISTICS OF A FRAME-SHAPED SUBSTRUCTURE

3.1 Introduction

In this chapter, the theoretical prediction of dynamic characteristics of a frame-shaped subcomponent is discussed. In industries, frame components are frequently applied to mechanical parts. Because it is cost-effective and can improve productivity, this structure is widely used in various industries. Nevertheless, a combination of beam shape components complicates the analysis of the dynamic behavior of the system. The complexity of the dynamic analysis originates from the vibrations of the assembled components, which affect other adjoining components by mode conversion at the joining point. When some types of vibratory motion, such as bending and torsional motion, pass through the structural joint, they affect other types according to the geometry of the joint and coupling angle. Dynamic properties are directly related to noise and vibration problems, which can affect customer satisfaction and the core performance of the product. Therefore, the dynamic analysis of mechanical systems is important in the development stage, and several

techniques have been studied to predict the dynamic behavior of complex structures. In this study, we introduce a simplified formulation to analyze the three-dimensional dynamic behaviors of a rigid frame structure. Based on the Euler–Bernoulli and Timoshenko–Ehrenfest beam theories, analytic solutions of six degree-of-freedom motions are defined using the boundary conditions at the end of each beam component and coupling constraints at the structural joint of the system. All equations are combined as a linearly united matrix equation that increases the scalability of the rigid frame model, and the motions are defined by the computed coefficient vector and external force vector.

3.2 Beam vibration theory

The three-dimensional behavior is a combination of six degree-of-freedom (DOF) motions at the axial position of the beam. As shown in Fig. 3.1, the vibratory motions of the beam system are composed of three translational motions based on the vertical deflection w, horizontal deflection v, and axial deformation u, and of three rotational motions based on the torsional angle θ, slope angle due to vertical bending φ, and horizontal bending ϕ. The vibratory behaviors of the beam structure are defined herein as the real parts of the general solution of the beam vibration, which are composed of trigonometric and hyperbolic basis functions. The 6-DOF motions of beam vibration are defined based on the Euler–Bernoulli and Timoshenko–Ehrenfest theories and are divided into two types according to the differential order of the governing equation [33].

The deflections and slope angles due to bending motions are defined as the solutions of fourth-order differential equations, and the general form of the solutions has four-basis functions and four coefficients, as shown in Eq. (3-1). The torsional angle and axial deformation are defined by a second-order equation with two-basis functions and two coefficients, as shown in Eq. (3-2).

$$f(x,t) = \left[\alpha_1 \cos\left(k_{f1}x\right) + \alpha_2 \sin\left(k_{f1}x\right) + \alpha_3 \cosh\left(k_{f2}x\right) + \alpha_4 \sinh\left(k_{f2}x\right)\right] e^{j\omega t} \quad (3\text{-}1)$$

$$g(x,t) = \left[\beta_1 \cos\left(k_g x\right) + \beta_2 \sin\left(k_g x\right)\right] e^{j\omega t} \quad (3\text{-}2)$$

For example, the vertical deflection w and the slope angle φ from the bending motions are defined as four-basis solutions by the theoretical governing equations. According to the Euler–Bernoulli theory, the vertical deflection is derived as a solution to Eq. (3-3) with the external vertical load q_b and the following properties of the beam: Young's modulus E, area moment of inertia I, volume density ρ, and cross-sectional area A. The slope angle is directly related to the bending deflection, as shown in Eq. (3-4), because of the theoretical assumption that the cross-section is always normal to the neutral axis of the beam. In contrast, for the Timoshenko–Ehrenfest theory, the bending motions are defined by Eqs. (3-5) and (3-6) with additional information on the shear modulus G and shear correction factor κ, which is formulated by Cowper [34]. The two equations can be combined as one governing equation (Eq. (3-7))

$$EI\frac{\partial^4 w}{\partial x^4} + \rho A\frac{\partial^2 w}{\partial t^2} = q_b(x,t) \tag{3-3}$$

$$\varphi = \frac{\partial w}{\partial x} \tag{3-4}$$

$$\rho A\frac{\partial^2 w}{\partial t^2} - \kappa GA\left(\frac{\partial^2 w}{\partial x^2} - \frac{\partial \varphi}{\partial x}\right) = q_b(x,t) \tag{3-5}$$

$$EI\frac{\partial^2 \varphi}{\partial x^2} + \kappa GA\left(\frac{\partial w}{\partial x} - \varphi\right) - \rho I\frac{\partial^2 \varphi}{\partial t^2} = 0 \tag{3-6}$$

$$EI\frac{\partial^4 w}{\partial x^4} + \rho A\frac{\partial^2 w}{\partial t^2} - \left(\rho I + \frac{\rho AEI}{\kappa GA}\right)\frac{\partial^4 w}{\partial x^2 \partial t^2} + \frac{\rho^2 AI}{\kappa GA}\frac{\partial^4 w}{\partial t^4} = 0 \tag{3-7}$$

From the governing equations, the wave number of the bending motions for each beam theory can be computed for the nonexternal load condition $q_b = 0$ as follows:

$$k_{b1} = k_{b2} = \sqrt[4]{\frac{\rho A}{EI}\omega^2} \tag{3-8}$$

$$k_{b1}, k_{b2} = \left|\frac{1}{2}\left(\frac{1}{C_s^2} + \frac{1}{C_l^2}\right)\omega^2 \pm \sqrt{\left(\frac{\omega}{C_l r_g}\right)^2 + \frac{1}{4}\left(\frac{1}{C_s^2} - \frac{1}{C_l^2}\right)^2 \omega^4}\right|^{\frac{1}{2}} \tag{3-9}$$

The wave number obtained from the Euler–Bernoulli theory in Eq. (3-8) can be simply computed using the material properties, and the wave number from the Timoshenko–Ehrenfest theory in Eq. (3-9) can be computed using the

radius of gyration $r_g = \sqrt{I/A}$ and the speeds of the shear wave $C_s = \sqrt{\kappa G/\rho}$ and longitudinal wave $C_l = \sqrt{E/\rho}$. Especially for the low-frequency range, the wave numbers of the Timoshenko–Ehrenfest theory converge to those of the Euler–Bernoulli theory because the oscillating frequency ω is negligible in Eq. (3-9).

The torsional angle θ and the axial deformation u are defined as two-basis solutions according to Eqs. (3-10) and (3-11), respectively, and the wave numbers are computed using Eqs. (3-12) and (3-13) for the nonexternal load condition, $q_\tau = 0$ and $q_f = 0$. For torsional motion, additional geometric properties of the beam components are applied: the polar moment of inertia I_p, and torsional constant J which is computable based on the shape of the cross-sectional area [35].

$$\rho I_p \frac{\partial^2 \theta}{\partial t^2} - GJ \frac{\partial^2 \theta}{\partial x^2} = q_\tau(x,t) \tag{3-10}$$

$$\rho A \frac{\partial^2 u}{\partial t^2} - EA \frac{\partial^2 u}{\partial x^2} = q_f(x,t) \tag{3-11}$$

$$k_\theta = \sqrt{\frac{\rho I_p}{GJ}} \tag{3-12}$$

$$k_u = \sqrt{\frac{\rho}{E}} \tag{3-13}$$

The general expressions of both the solution types in Eqs. (3-1) and (3-2) can be rewritten as a product of the basis and coefficient vectors as follows:

$$f(x,t) = \left[\cos(k_{f1}x)\ \sin(k_{f1}x)\ \cosh(k_{f2}x)\ \sinh(k_{f2}x)\right]\begin{bmatrix}\alpha_1\\ \alpha_2\\ \alpha_3\\ \alpha_4\end{bmatrix} e^{j\omega t} = \mathbf{X}\mathbf{A}e^{j\omega t} \quad (3\text{-}14)$$

$$g(x,t) = \left[\cos(k_g x)\ \sin(k_g x)\right]\begin{bmatrix}\beta_1\\ \beta_2\end{bmatrix} e^{j\omega t} = \mathbf{Y}\mathbf{B}e^{j\omega t} \quad (3\text{-}15)$$

3.2.1 Linear algebraic expression

The four-basis solutions can be expressed by Eq. (3-14) and the two-basis solutions in Eq. (3-15). The basis vector $\mathbf{X}$ and coefficient vector $\mathbf{A}$ are row and column vectors with four elements, respectively, and vectors $\mathbf{Y}$ and $\mathbf{B}$ are the same with two elements, respectively. Total 6-DOF deformations of the beam component are arranged as a product of deformation basis matrix and total coefficient vector as shown in Eq. (3-16). The total coefficient vector consists of four element coefficient vectors, which are coefficient vectors of vertical bending motions $\mathbf{A_w}$, $\mathbf{A_\varphi}$, and horizontal bending motions $\mathbf{A_v}$, $\mathbf{A_\phi}$, and two element coefficient vectors, which are torsional motion $\mathbf{B_\theta}$ and axial deformation $\mathbf{B_u}$. Further, the deformation basis matrix contains the basis vectors of each 6-DOF motions which are $\mathbf{X_w}$, $\mathbf{X_\varphi}$, $\mathbf{X_\theta}$, $\mathbf{X_v}$, $\mathbf{X_\phi}$, and $\mathbf{X_u}$.

$$\begin{bmatrix} w(x,t) \\ \varphi(x,t) \\ \theta(x,t) \\ v(x,t) \\ \phi(x,t) \\ u(x,t) \end{bmatrix} = \begin{bmatrix} \mathbf{X_w} & & & & & \\ & \mathbf{X_\varphi} & & & & \\ & & \mathbf{Y_\theta} & & & \\ & & & \mathbf{X_v} & & \\ & & & & \mathbf{X_\phi} & \\ & & & & & \mathbf{Y_u} \end{bmatrix} \begin{bmatrix} \mathbf{A_w} \\ \mathbf{A_\varphi} \\ \mathbf{B_\theta} \\ \mathbf{A_v} \\ \mathbf{A_\phi} \\ \mathbf{B_u} \end{bmatrix} \tag{3-16}$$

According to both beam theories, the slope angle of the bending motion has a certain relationship with the deformation of bending motion. To represent the relationship between the deflection w and slope angle φ, the proportion matrix $\boldsymbol{\mu_w}$ is proposed herein, as shown in Eq. (3-17).

$$\mathbf{X_\varphi A_\varphi} = \mathbf{X_w \mu_w A_w} \tag{3-17}$$

To simplify the proportion matrix $\boldsymbol{\mu_w}$, derivative matrixes $\mathbf{D_4}$ and $\mathbf{D_2}$ are introduced, and the derivative of the basis function vector can be expressed as the linear product of the basis function vector and derivative matrix because of the cyclic nature of the derivation of the trigonometric and hyperbolic bases.

$$\frac{\partial}{\partial x}\mathbf{X} = [\cos(k_1 x)\ \sin(k_1 x)\ \cosh(k_2 x)\ \sinh(k_2 x)] \begin{bmatrix} 0 & k_1 & 0 & 0 \\ -k_1 & 0 & 0 & 0 \\ 0 & 0 & 0 & k_2 \\ 0 & 0 & k_2 & 0 \end{bmatrix} = \mathbf{XD_4} \tag{3-18}$$

$$\frac{\partial}{\partial x}\mathbf{Y} = [\cos(kx)\ \sin(kx)] \begin{bmatrix} 0 & k \\ -k & 0 \end{bmatrix} = \mathbf{YD_2} \tag{3-19}$$

The derivative matrix $\mathbf{D_4}$ in Eq. (3-18) is applied to the four-basis vector, and $\mathbf{D_2}$ in Eq. (3-19) is applied to the two-basis vector. By combining the derivative matrix $\mathbf{D_4}$ with Eqs. (3-4) and (3-5), the proportion matrix $\boldsymbol{\mu}_\mathbf{w}$ can be computed as Eqs. (3-20) and (3-21), respectively, for the Euler–Bernoulli and Timoshenko–Ehrenfest theories.

$$\boldsymbol{\mu}_{\mathbf{w,EB}} = \mathbf{D}_{\mathbf{4,w}} \tag{3-20}$$

$$\boldsymbol{\mu}_{\mathbf{w,TE}} = \mathbf{D}_{\mathbf{4,w}}^{-\mathbf{1}} \left[\left(\frac{\omega}{C_S} \right)^2 \mathbf{I_4} + \mathbf{D}_{\mathbf{4,w}}^{\mathbf{2}} \right] \tag{3-21}$$

Using the proportion matrix $\boldsymbol{\mu}_\mathbf{w}$, the entire 6-DOF motion of a beam component is combined with the deformed basis matrix $\mathbf{X}_{\boldsymbol{\mu}}$, which contains basis vectors and proportional matrixes, and total coefficient vector $\mathbf{A_t}$ as in Eq. (3-22). In this form, the number of elements of total coefficient vector $\mathbf{A_t}$, which need to be defined, is reduced from 20 to 12 since the deformation and slope angle of bending motion share the coefficients based on the relationship expressed by proportion matrix $\boldsymbol{\mu}_\mathbf{w}$ and $\boldsymbol{\mu}_\mathbf{v}$.

$$\mathbf{X_\mu A_t} = \begin{bmatrix} w(x,t) \\ \varphi(x,t) \\ \theta(x,t) \\ v(x,t) \\ \phi(x,t) \\ u(x,t) \end{bmatrix} = \begin{bmatrix} \mathbf{X_w} & & & & & \\ & \mathbf{X_w} & & & & \\ & & \mathbf{Y_\theta} & & & \\ & & & \mathbf{X_v} & & \\ & & & & \mathbf{X_v} & \\ & & & & & \mathbf{Y_u} \end{bmatrix} \begin{bmatrix} \mathbf{I_4} & & & & & \\ \boldsymbol{\mu_w} & & & & & \\ & \mathbf{I_2} & & & & \\ & & \mathbf{I_4} & & & \\ & & & \boldsymbol{\mu_v} & & \\ & & & & \mathbf{I_2} & \end{bmatrix} \begin{bmatrix} \mathbf{A_w} \\ \mathbf{B_\theta} \\ \mathbf{A_v} \\ \mathbf{B_u} \end{bmatrix} \tag{3-22}$$

According to the two beam theories, the internal forces, including the axial tension F, torsional torque T, vertical shear force V_w and vertical moment M_w, are related to the motions as follows:

$$V_w(x) = -EI\frac{\partial^3 w}{\partial x^3} = (-EI)\mathbf{X_w D_{4,w}^3 A_w} \tag{3-23}$$

$$M_w(x) = EI\frac{\partial^2 w}{\partial x^2} = (EI)\mathbf{X_w D_{4,w}^2 A_w} \tag{3-24}$$

$$V_w(x) = \kappa GA\left[\frac{\partial w}{\partial x} - \varphi\right] = (\kappa GA)\mathbf{X_w}\left[\mathbf{D_{4,w}} - \boldsymbol{\mu_w}\right]\mathbf{A_w} \tag{3-25}$$

$$M_w(x) = EI\frac{\partial \varphi}{\partial x} = (EI)\mathbf{X_w D_{4,w}}\boldsymbol{\mu_w}\mathbf{A_w} \tag{3-26}$$

$$T(x) = G\gamma\frac{\partial \theta}{\partial x} = (G\gamma)\mathbf{Y_\theta D_{2,\theta} B_\theta} \tag{3-27}$$

$$F(x) = EA\frac{\partial u}{\partial x} = (EA)\mathbf{Y_u D_{2,u} B_u} \tag{3-28}$$

The shear force and bending moment are related to the four-basis solutions, deflection, and the slope angle of the bending motion. The shear force and bending moment derived from Euler–Bernoulli theory are shown in Eqs. (3-23)

and (3-24), and those derived from the Timoshenko–Ehrenfest theory are shown in Eqs. (3-25) and (3-26), respectively. In addition, the torque and axial force are related to the two-basis solutions, torsional angle, and axial deformation, as shown in Eqs. (3-27) and (3-28), respectively.

Similarly, the internal force matrix $\mathbf{F_i}$ in Eqs. (3-23)–(3-28) can be combined into a force basis matrix $\mathbf{X_F}$ with the rigidity matrix $\mathbf{R}$, force-derivative matrix $\boldsymbol{\lambda}$ and coefficient vector $\mathbf{A_t}$ as shown in Eq. (3-29). The rigidity matrix and force-derivative matrix are described in Eqs. (3-30) and (3-31), each representing the Euler–Bernoulli and Timoshenko–Ehrenfest theories.

$$\mathbf{F_i} = \begin{bmatrix} V_w \\ M_w \\ T \\ V_v \\ M_v \\ F \end{bmatrix} = \begin{bmatrix} \mathbf{X_w} & & & & & \\ & \mathbf{X_w} & & & & \\ & & \mathbf{Y_\theta} & & & \\ & & & \mathbf{X_v} & & \\ & & & & \mathbf{X_v} & \\ & & & & & \mathbf{Y_u} \end{bmatrix} \mathbf{R}\boldsymbol{\lambda}\mathbf{A_t} = \mathbf{X_F}\mathbf{A_t} \tag{3-29}$$

$$\mathbf{R_{Euler}} = \begin{bmatrix} (EI)\mathbf{I_4} & & & & & \\ & (EI)\mathbf{I_4} & & & & \\ & & (G\gamma)\mathbf{I_2} & & & \\ & & & (EI)\mathbf{I_4} & & \\ & & & & (EI)\mathbf{I_4} & \\ & & & & & (EA)\mathbf{I_2} \end{bmatrix}$$

$$\boldsymbol{\lambda}_{\mathbf{Euler}} = \begin{bmatrix} -\mathbf{D}^3_{4,\mathbf{w}} & & & & \\ \mathbf{D}^2_{4,\mathbf{w}} & & & & \\ & \mathbf{D}_{2,\boldsymbol{\theta}} & & & \\ & & -\mathbf{D}^3_{4,\mathbf{v}} & & \\ & & \mathbf{D}^2_{4,\mathbf{v}} & & \\ & & & \mathbf{D}_{2,\mathbf{u}} & \end{bmatrix} \tag{3-30}$$

$$\mathbf{R}_{\mathbf{Timoshenko}} = \begin{bmatrix} (\kappa GA)\mathbf{I_4} & & & & & \\ & (EI)\mathbf{I_4} & & & & \\ & & (G\gamma)\mathbf{I_2} & & & \\ & & & (\kappa GA) & & \\ & & & & (EI)\mathbf{I_4} & \\ & & & & & (EA)\mathbf{I_2} \end{bmatrix} \tag{3-31}$$

$$\boldsymbol{\lambda}_{\mathbf{Timoshenko}} = \begin{bmatrix} \mathbf{D_{4,w}} - \boldsymbol{\mu}_{\mathbf{w}} & & & & & \\ \mathbf{D_{4,w}}\boldsymbol{\mu}_{\mathbf{w}} & & & & & \\ & \mathbf{D_{2,\theta}} & & & & \\ & & \mathbf{D_{4,v}} - \boldsymbol{\mu}_{\mathbf{v}} & & & \\ & & \mathbf{D_{4,v}}\boldsymbol{\mu}_{\mathbf{v}} & & & \\ & & & & \mathbf{D_{2,u}} & \end{bmatrix}$$

3.2.2 Dynamics at the boundaries

The dynamic behavior of a rigid frame structure is defined by several boundary conditions at the ends of the beam elements, known as the compatibility and force equilibrium conditions that have a number equal to the DOF of the structure [36]. To derive general boundary conditions of the beam system, a diagram of an infinitesimal element at a specific location in a beam component is shown in Fig. 3.2.

The infinitesimal element receives several internal forces, including shear force, bending moment, longitudinal tension, and torque from the beam itself, which are arranged in Eq. (3-29), and the external force from 6-DOF spring which connects the beam structure to the external system. The equation of the force equilibrium condition is expressed by Eq. (3-32) using the inertia matrix $\mathbf{M_i}$ and acceleration of the 6-DOF motion $\mathbf{a_i}$ of the element, sum of internal

forces from both sides $\Sigma\mathbf{F_i}$, stiffness of 6-DOF spring $\mathbf{s}$, and dynamic motions of the element $\mathbf{W_i}$ and outer system $\mathbf{W_o}$.

$$\mathbf{M_i a_i} = \Sigma\mathbf{F_i} + \mathbf{s}(\mathbf{W_i} - \mathbf{W_o}) \tag{3-32}$$

For an infinitesimal volume, the inertia matrix is negligible so that the left-hand side of Eq. (3-32) converges to zero. Therefore, the dynamic behavior of the system is defined according to the stiffness matrix. If the stiffness term is infinity, and the main system characteristic is that the 6-DOF motions of the infinitesimal element are equal to the motions of the external system, that is, $\mathbf{W_i} = \mathbf{W_o}$. Conversely, the zero stiffness of the spring means that the elastic force from the relative deformation between the element and outer system; in other words, the internal force term goes to zero, $\Sigma\mathbf{F_i} = \mathbf{0}$. When there is no beam on one side of the element, the preceding two conditions coincide with the fixed-end and free-end conditions, respectively.

3.2.3 Dynamics at the joint

The composition of the structural joint of the rigid frame structure is shown in Fig. 3.3. Similar to the dynamics at the boundaries in chapter 3.2.2, the force equilibrium equations of the coupling point are expressed by Eq. (3-

33) with the inertia matrix $\mathbf{M_J}$, which contains mass m_j and mass moment of inertia I_{xx}, I_{yy} and I_{zz}, and acceleration of the 6-DOF motion $\mathbf{a_J}$ of the joint, and internal forces $\mathbf{F_i}$ from both sides of the beam components:

$$\mathbf{M_J a_J} = \begin{bmatrix} m_j & & & & & \\ & I_{yy} & & & & \\ & & I_{xx} & & & \\ & & & m_j & & \\ & & & & I_{zz} & \\ & & & & & m_j \end{bmatrix} \begin{bmatrix} a_w \\ a_\varphi \\ a_\theta \\ a_v \\ a_\phi \\ a_u \end{bmatrix} = \mathbf{F_{ja}} + \mathbf{F_{jb}} \qquad (3\text{-}33)$$

To reflect the conversion of the vibration mode by the joint geometry and coupling angle, the motions and internal forces at the joint location were adjusted by the geometry matrix and rotation matrix. The geometry matrix reflects the distance $[x_d, y_d, z_d]$, which is the displacement from the center of gravity of the joint mass to the geometric center of the cross-sectional area of the beam component at the contact position. The geometric matrixes $\mathbf{Z_X}$ and $\mathbf{Z_F}$ in Eq. (3-34) are necessary to adjust the motions $\mathbf{X_t}$ and the internal forces $\mathbf{F_i}$ of the ends of either side of the beams to the motions $\mathbf{X_J} = \mathbf{Z_X X_t}$ and the internal forces $\mathbf{F_J} = \mathbf{Z_F F_i}$ at the center of structural joint, following the local rigidity assumption of the joint. The rotation matrix changes the directions of motion and converges the types of internal forces according to the coupling angle of the rigid frame structure. To reflect the rotated angle of the beam

component to the global coordinates, a different rotation matrix $\mathbf{T}$ is required for each beam for azimuth angle ψ and elevation angle ξ, which is expressed as Eq. (3-35).

$$\mathbf{Z_X} = \begin{bmatrix} 1 & -x_d & -y_d & & & \\ & 1 & & & & \\ & & 1 & & & \\ & & z_d & 1 & -x_d & \\ & & & & 1 & \\ & z_d & & & y_d & 1 \end{bmatrix}, \quad \mathbf{Z_F} = \begin{bmatrix} 1 & & & & & \\ x_d & 1 & & & & -z_d \\ y_d & & 1 & -z_d & & \\ & & & 1 & & \\ & & & x_d & 1 & -y_d \\ & & & & & 1 \end{bmatrix} \quad (3\text{-}34)$$

$$\mathbf{T} = \begin{bmatrix} 1 & & & & & \\ & cos\psi & -sin\psi & & & \\ & sin\psi & cos\psi & & & \\ & & & cos\psi & & -sin\psi \\ & & & & 1 & \\ & & & sin\psi & & cos\psi \end{bmatrix} \begin{bmatrix} cos\xi & & & & & sin\xi \\ & 1 & & & & \\ & & cos\xi & & sin\xi & \\ & & & 1 & & \\ & & -sin\xi & & cos\xi & \\ -sin\xi & & & & & cos\xi \end{bmatrix} \quad (3\text{-}35)$$

The dynamic characteristics of the vibrating beam are defined by the equation of motion at the joint and boundary constraints. At each end position of the rigid frame structure in Fig. 3.3, $x_a = 0$ and $x_b = L_b$, the internal forces are equal to the external forces $\mathbf{F_e}$ at the same position, as in Eq. (3-36). The motions at the geometrical center of the joint can be expressed with the motion of each beam component at coupling positions, $x_a = L_a$ and $x_b = 0$, respectively, and the compatibility condition is established, as shown in Eq. (3-37). The equations of motion for the 6-DOF motions of the structural joint are formulated using a joint inertia matrix $\mathbf{M_J}$ and internal forces from the beam on each side, as shown in Eq. (3-38).

$$\mathbf{T_a X_{F,a0} A_{t,a}} = \mathbf{F_{e,a0}},\ \mathbf{T_b X_{F,bL} A_{t,b}} = \mathbf{F_{e,bL}} \tag{3-36}$$

$$\mathbf{Z_{Xa} T_a X_{\mu,aL} A_{t,a}} = \mathbf{Z_{Xb} T_b X_{\mu,b0} A_{t,b}} \tag{3-37}$$

$$-\omega^2 \mathbf{M_J Z_{Xa} T_a X_{\mu,aL} A_{t,a}} = -\mathbf{Z_{Fa} T_a X_{F,aL} A_{t,a}} + \mathbf{Z_{Fb} T_b X_{F,b0} A_{t,b}} + \mathbf{F_{e,J}} \tag{3-38}$$

The three-dimensional behaviors of the rigid frame structures are fully defined by solving the simultaneous equations in Eqs. (3-36)– (3-38), which are arranged as follows [37]:

$$\begin{bmatrix} \mathbf{T_a X_{F,a0}} & \mathbf{0} \\ \mathbf{Z_{Xa} T_a X_{\mu,aL}} & -\mathbf{Z_{Xb} T_b X_{\mu,b0}} \\ -\omega^2 \mathbf{M_J Z_{Xa} T_a X_{\mu,aL}} + \mathbf{Z_{Fa} T_a X_{F,aL}} & -\mathbf{Z_{Fb} T_b X_{F,b0}} \\ \mathbf{0} & \mathbf{T_b X_{F,bL}} \end{bmatrix} \begin{bmatrix} \mathbf{A_{t,a}} \\ \mathbf{A_{t,b}} \end{bmatrix} = \begin{bmatrix} \mathbf{F_{e,a0}} \\ \mathbf{0} \\ \mathbf{F_{e,J}} \\ \mathbf{F_{e,bL}} \end{bmatrix} \tag{3-39}$$

Consequently, the dynamic behavior of the rigid frame structure is determined by the linear algebraic formulation of $\mathbf{C_{ov} A_{ov}} = \mathbf{F_{e,ov}}$ with the overall coefficient vector $\mathbf{A_{ov}} = \left[\mathbf{A_{t,a}}\ \mathbf{A_{t,b}}\right]^{\mathrm{T}}$, which can be calculated using the overall characteristic matrix $\mathbf{C_{ov}}$ and the external force vector $\mathbf{F_{e,ov}} = \left[\mathbf{F_{e,a0}}\ \mathbf{0}\ \mathbf{F_{e,J}}\ \mathbf{F_{e,bL}}\right]^{\mathrm{T}}$ on the right-hand side of Eq. (3-39). The response of the system becomes intense at a certain frequency where $\mathbf{C_{ov}}$ has a singularity, which means that a vibration mode exists at that frequency. Thus, the modal

frequencies can be computed using the determinant of the overall characteristic matrix.

This linear algebraic expression offers additional advantages in the expansion and the modification of the structure. If another beam component, beam C, is added at the end position of beam B, the characteristic matrix $\mathbf{C_{ov}}$ can be simply formulated as shown in Eq. (3-40). Similarly, in the case of joining two beams, the compatibility conditions and equilibrium conditions of the joints at each end position of beam B; free boundary conditions at the opposite ends of beam A and C constitute the total characteristic equation of the rigid frame structure of three beams. With the overall coefficient vector $\mathbf{A_{ov}} = \left[\mathbf{A_{t,a}}\ \mathbf{A_{t,b}}\ \mathbf{A_{t,c}}\right]^{\mathrm{T}}$ and the external force vector $\mathbf{F_{e,ov}} = \left[\mathbf{F_{e,a0}}\ \mathbf{0}\ \mathbf{F_{e,J1}}\ \mathbf{0}\ \mathbf{F_{e,J2}}\ \mathbf{F_{e,cL}}\right]^{\mathrm{T}}$, the dynamic behaviors of this structure can be simply computed as a solution of the linear algebraic formulation. In addition, for the other case of structural modification where beam C is connected at the same joint of beam A and B, the calculation process remains unchanged, and only the characteristic matrix $\mathbf{C_{ov}}$ needs to be changed to the same as Eq. (3-41).

$$\mathbf{C_{ov}} =$$

$$\begin{bmatrix} \mathbf{T_a X_{F,a0}} & \mathbf{0} & \mathbf{0} \\ \mathbf{Z_{Xa} T_a X_{\mu,aL}} & \mathbf{-Z_{Xb1} T_b X_{\mu,b0}} & \mathbf{0} \\ \mathbf{-\omega^2 M_{J1} Z_{Xa} T_a X_{\mu,aL} + Z_{Fa} T_a X_{F,aL}} & \mathbf{-Z_{Fb1} T_b X_{F,b0}} & \mathbf{0} \\ \mathbf{0} & \mathbf{Z_{Xb2} T_b X_{\mu,bL}} & \mathbf{-Z_{Xc} T_c X_{\mu,c0}} \\ \mathbf{0} & \mathbf{-\omega^2 M_{J2} Z_{Xb2} T_b X_{\mu,bL} + Z_{Fb2} T_b X_{F,bL}} & \mathbf{-Z_{Fc} T_c X_{F,c0}} \\ \mathbf{0} & \mathbf{0} & \mathbf{T_c X_{F,cL}} \end{bmatrix} \quad (3\text{-}40)$$

$$\mathbf{C_{ov}} = \begin{bmatrix} \mathbf{T_a X_{F,a0}} & \mathbf{0} & \mathbf{0} \\ \mathbf{Z_{Xa} T_a X_{\mu,aL}} & \mathbf{-Z_{Xb1} T_b X_{\mu,b0}} & \mathbf{0} \\ \mathbf{-\omega^2 M_{J1} Z_{Xa} T_a X_{\mu,aL} + Z_{Fa} T_a X_{F,aL}} & \mathbf{-Z_{Fb1} T_b X_{F,b0}} & \mathbf{-Z_{Fc} T_c X_{F,c0}} \\ \mathbf{0} & \mathbf{T_b X_{F,bL}} & \mathbf{0} \\ \mathbf{Z_{Xa} T_a X_{\mu,aL}} & \mathbf{0} & \mathbf{-Z_{Xc} T_c X_{\mu,c0}} \\ \mathbf{0} & \mathbf{0} & \mathbf{T_c X_{F,cL}} \end{bmatrix} \quad (3\text{-}41)$$

3.3 Experimental verification

The analytically solved dynamic behavior of the rigid frame structure was verified by testing the modal parameters using the experimental modal analysis (EMA) method. Four structures were verified, in which three beam components, named beams A, B and C, were combined in different shapes. The beam components have identical material properties with Young's modulus of 210 KN·mm2, Poisson's ratio of 0.3, and volume mass density of 7850 kg·m3, which are well-known properties of alloy steel. Moreover, for the geometric figures, the thickness of the three components is equal being 30 mm; and the length and width of each component are listed as follows: beam A, B and C are 200 mm, 150 mm and 170 mm long, respectively; and have a width of 40.0 mm, 34.6 mm and 28.3 mm, respectively. The four test cases were organized with these three beams shown in Fig. 3.4. Case 1 was composed of beam A and B which were coupled at a 30° angle, and Case 2 was composed of beam A and C with a 45° coupling angle. Case 3 was a linearly combined structure of three beam components, where beam B and C were joined to both sides of beam A with 30° and 45° coupling angles, respectively, for each joint. Case 4 was a three-beam-combined structure in which three components are coupled at single joining points like wishbone. In this case, beam B was coupled at 30°

angle like case 1, and beam C was coupled at the same joining points as right angles downward to beam A, which was the opposite direction to beam B.

Frequency responses of rigid frame structures were tested using the EMA method with the tri-axial accelerometers (356A15, PCB Piezotronic) and impact hammer (Type 8206-002, Brüel & Kjær). In general, when using attachable sensors for modal analysis, it is empirically recommended that the weight of the sensors be less than one tenth of that of the test sample, and the frequency shift due to mass loading effect be less than 5% of frequency of each mode [38]. Between 10 and 14 accelerometers, each weighing 9.5 g, were used, and the total weight was less than 3.0% of the weight of the structure. The observed frequency shift was a maximum of 4.8% and an average of 3.1%, confirming that suitable sensors were used for this EMA experiment. Modal parameters were analyzed using the LMS Test.Lab software of Siemens industry. The analytical modal frequencies of the corresponding rigid frame model were calculated separately using the proposed formulation in chapter 3.2.3, based on the Euler–Bernoulli and Timoshenko–Ehrenfest beam theories.

The frequency responses of the four cases were measured and computed in free-free boundary conditions, and all estimated modal frequencies are listed in Tables 3.1–3.4. EMA in Tables represents the test results using EMA method, and EB and TE represent the analyzed singular frequencies according to the

Euler–Bernoulli and Timoshenko–Ehrenfest beam theories, respectively. The estimated modes were the first three modes of the out-of-plane and in-plane modes of the rigid frame models. For the dynamic behavior estimation, the analytic calculation based on the two beam theories predicted the modal frequencies with mean error rates of less than 8%. Meanwhile, the Timoshenko–Ehrenfest beam theory showed lower error rates compared to the Euler–Bernoulli beam theory, which exhibited mean absolute percentage errors (MAPE), 4.3% and 7.6%, respectively for each theory averaging all four cases for experimental verification.

Figs. 3.5–3.7 depict first six mode shapes of four test cases. The shape of each mode of Case 1 and Case 2 is a two-beam coupled model and is identical in both cases (Fig. 3.5). In these cases, the first three mode shapes of out-of-plane and in-plane modes are the first, second, and third bending modes common in beam structures under free-free boundary conditions. The first three mode shapes of in-plane modes of Case 3 shown in Fig. 3.6 are similar to Case 1 and Case 2, whereas the first three mode shapes of out-of-plane modes have different shapes from the previous cases because of the complexity of the structural shape. The first and third out-of-plane mode of Case 3 are the common first and second torsional modes of the beam structure respectively, and the second out-of-plane mode appears as a converged mode of first bending

mode and rotational mode. The second mode shape of Case 3 is considered as a result of erroneous analysis; however, but the EMA test procedure yields an almost identical shape as well. The mode shapes of Case 4 are shown in Fig. 3.7. The mode shapes of Case 4 exhibit asymmetric planar characteristics because the beam extends from the central joint. The first out-of-plane mode of Case 4 seems like bumping mode of the plane formed by the three beams, and the second and third out-of-plane mode are second bending modes for different direction for the structure. And the first and second mode shapes of in-plane are bending modes for different direction and the third in-plane mode shape is seems like twist mode of circular plane.

The similarity between the mode shape of the EMA method and the mode shape computed using the formula proposed in chapter 3.2.3 is checked using the Modal Assurance Criterion (MAC). The MAC is a value indicating how correlated two modal vectors are [39]. MAC value ranges from 0 to 1 with 0 indicating zero similarity between two modal vectors and 1 indicating that the two modes are identical. The MAC values of two modal vectors, $\boldsymbol{\Phi_1}$ and $\boldsymbol{\Phi_2}$, are computed using the following formula in Eq. (3-42).

$$MAC = \frac{\left|\boldsymbol{\Phi_1^T \Phi_2}\right|^2}{\left(\boldsymbol{\Phi_1^T \Phi_1}\right)\left(\boldsymbol{\Phi_2^T \Phi_2}\right)} \tag{3-42}$$

Ideally, MAC values should be computed as 1 for diagonal and 0 for off-diagonal components; however, such ideal results are impractical due to errors in the EMA test caused by physical limitations such as attaching sensors by hand or slanted excitation when using an impact hammer. The MAC values between modal vectors from EMA results and analytic solutions are listed in Tables 3.5–3.8 and Figs. 3.8–3.11. In the figure and table of MAC values, mode 1–3 are the first three out-of-plane modes, and mode 4–6 are the first three in-plane modes, respectively. Diagonal values in Tables 5–8 show a high similarity of mode shapes between EMA results and analytic solutions, which are computed using the proposed linear algebraic expression. All the diagonal components of MAC tables are higher than 0.8, which indicates a high similarity of the mode shapes corresponding to each other, and they behave in almost the identical shape. Simultaneously, low MAC values of the off-diagonal components are also satisfied to be less than 0.2, which means that the non-corresponding modes are independent and not correlated with each other. As a result, the validity of the dynamic behavior analysis using the proposed formulation was verified through accurate computation of vibrating mode shapes.

As a result of these verification procedures, the proposed predictive method with linear algebraic formulation showed a high overall accuracy for

predicting the dynamic behaviors of rigid frame structures using both beam theories. Furthermore, the Timoshenko–Ehrenfest theory predicted the behaviors better than the Euler–Bernoulli theory by comparing error rate of estimated modal frequencies, and the overall predicted frequencies using the Timoshenko–Ehrenfest theory showed higher values than when using the Euler–Bernoulli theory. This result is expected according to the assumption of the Euler–Bernoulli beam theory, which excludes the effect of rotational distortion between the cross-sectional area and the mid-plane of the beam components. Therefore, the analysis based on the Timoshenko–Ehrenfest beam theory is suitable for the estimation of dynamic behaviors of rigid frame structures.

3.4 Result and discussion

In this study, the three-dimensional dynamic behavior of a rigid frame structure was analytically solved, and a linear algebraic formulation was introduced to simplify the calculations. The 6-DOF motions of the system were derived based on the Euler–Bernoulli theory and Timoshenko–Ehrenfest theory and were defined by the physical conditions of the structural joint and the end position of the coupled structure. The derived equations were converted into matrix form using introduced derivative matrix and arranged as simple matrix equations, which consisted of a characteristic matrix, coefficient vector, and external force vector. Then, dynamic behaviors of the rigid frame structure were computed simply by solving the linear algebraic formulation, $\mathbf{CA} = \mathbf{F}$. The modal frequencies can be investigated as a singular point of the determinant of the characteristic matrix, and all 6-DOF behaviors can be defined by the computed coefficients and the given external forces. Finally, verification test was conducted to compare the estimated modal parameters of the analytical calculation and experimentally measured values. The consistency of the predicted vibration modes was confirmed using MAC values, and the error rates between predicted and tested modal frequencies were computed and used as verification indicators. The Euler–Bernoulli and Timoshenko–Ehrenfest theories were equally applied for analytic calculations, and both predicted

results showed high accuracies with mean error rates less than 8%. Furthermore, we verified that the Timoshenko–Ehrenfest theory has higher accuracy, below 5% of MAPE, than the Euler–Bernoulli theory for estimating the dynamic behavior of a rigid frame structure.

The primary advantage of a linear algebraic formulation is the convenience of calculation, as mentioned in Section 1. Based on the cyclical nature of the derivative of the basis functions, the solution can be represented as a product of the derivative matrix and basis vector, which unites all equations of the boundary conditions and coupling constraints as a linear algebraic form of matrixes. With this simple form of characteristic equations, dynamic behaviors of the rigid frame structure were computed by a simple inverse matrix calculation of the characteristic matrix instead of solving series of differential equations. Another advantage was the flexibility for the modification of the target model to be analyzed. For a structural modification such as the additional connection with another beam component, the form of linear algebraic formulation remains unchanged as $\mathbf{CA} = \mathbf{F}$, and the coefficient vector and external force vector just increases in size according to the DOF of dynamic behavior of the structure. Only the composition of the characteristic matrix is modified following the coupling condition of beam components, as shown in Section 2.3. Dynamic behaviors of four structures in which the same

components are combined in different shapes were easily computed using the proposed formulation, and the accuracy of analytic solution was verified compared to the experimental result in Section 3. Although this study is limited to rigid frame structure where all subcomponents are beam-shaped, the modeling can be expanded in future studies based on the theory to various parts such as plates and huge masses. Consequently, considering this convenience and the high associated accuracy, the predictive method proposed here can be effectively used to estimate the three-dimensional dynamic behaviors of rigid frame structures.

TABLE 3.1 Measured and estimated modal frequencies of the rigid frame model, Case 1

	Out-of-plane mode [Hz]			in-plane mode [Hz]			MAPE
	1st	2nd	3rd	1st	2nd	3rd	
EMA	1556.5	3121.3	5709.3	1363.4	3808.9	6250.7	-
EB	1650.7	3282.5	6303.2	1503.6	4133.5	6820.8	7.6%
TE	1619.0	3093.3	5707.4	1456.5	3752.3	6302.9	2.2%

TABLE 3.2 Measured and estimated modal frequencies of the rigid frame model, Case 2

	Out-of-plane mode [Hz]			in-plane mode [Hz]			MAPE
	1st	2nd	3rd	1st	2nd	3rd	
EMA	1783.0	2761.4	4948.4	998.2	3190.4	4913.2	-
EB	1905.9	2814.1	5328.4	1114.2	3283.8	5484.8	6.5%
TE	1875.2	2666.5	4952.6	1093.0	3056.8	5054.7	3.9%

TABLE 3.3 Measured and estimated modal frequencies of the rigid frame model, Case 3

	Out-of-plane mode [Hz]			in-plane mode [Hz]			MAPE
	1st	2nd	3rd	1st	2nd	3rd	
EMA	1165.6	1479.0	2784.7	603.0	1420.0	3036.2	-
EB	1247.3	1536.9	2885.7	638.6	1574.1	3200.0	5.7%
TE	1219.8	1517.9	2737.6	632.6	1525.7	2985.1	3.6%

TABLE 3.4 Measured and estimated modal frequencies of the rigid frame model, Case 4

	Out-of-plane mode [Hz]			in-plane mode [Hz]			MAPE
	1st	2nd	3rd	1st	2nd	3rd	
EMA	1064.2	2142.6	2686.0	771.1	1103.6	3131.7	-
EB	1219.1	2323.1	2927.6	869.6	1317.9	3402.2	10.7%
TE	1193.2	2248.5	2809.2	864.7	1294.6	3162.5	7.6%

TABLE 3.5 MAC table between 6 modes from EMA test and analytic solution, Case 1

	Out-of-plane mode			in-plane mode		
	Mode 1	Mode 2	Mode 3	Mode 4	Mode 5	Mode 6
Mode 1	0.955	6.06e-03	6.34e-02	2.19e-03	6.94e-05	1.25e-04
Mode 2	6.38e-08	0.954	1.36e-03	6.09e-05	4.00e-05	3.97e-07
Mode 3	9.27e-02	5.65e-03	0.953	1.66e-04	9.04e-05	4.15e-04
Mode 4	2.01e-03	1.24e-05	1.78e-04	0.995	1.29e-02	1.08e-01
Mode 5	8.86e-06	2.26e-05	1.94e-07	3.31e-03	0.995	2.78e-03
Mode 6	1.85e-05	1.12e-05	1.15e-04	1.23e-01	1.24e-02	0.991

TABLE 3.6 MAC table between 6 modes from EMA test and analytic solution, Case 2

	Out-of-plane mode			in-plane mode		
	Mode 1	Mode 2	Mode 3	Mode 4	Mode 5	Mode 6
Mode 1	0.916	1.96e-03	4.92e-03	5.46e-05	1.84e-04	6.59e-06
Mode 2	8.57e-04	0.939	2.22e-02	2.81e-07	2.34e-05	7.71e-06
Mode 3	5.04e-02	2.33e-02	0.962	5.54e-04	3.49e-04	4.14e-03
Mode 4	6.95e-06	2.97e-08	1.70e-05	0.995	3.53e-02	1.37e-01
Mode 5	1.54e-06	4.70e-05	2.21e-07	4.14e-02	0.994	4.17e-02
Mode 6	8.15e-03	3.36e-03	1.60e-01	1.37e-01	3.30e-02	0.833

TABLE 3.7 MAC table between 6 modes from EMA test and analytic solution, Case 3

	Out-of-plane mode			in-plane mode		
	Mode 1	Mode 2	Mode 3	Mode 4	Mode 5	Mode 6
Mode 1	0.981	9.14e-04	2.65e-04	6.26e-07	3.08e-05	3.31e-06
Mode 2	1.59e-04	0.916	4.60e-02	1.85e-04	5.16e-02	5.06e-07
Mode 3	1.91e-03	2.40e-02	0.941	5.48e-06	6.85e-06	1.68e-05
Mode 4	1.21e-04	4.22e-05	2.62e-05	0.998	1.34e-02	1.82e-01
Mode 5	3.45e-04	1.50e-01	9.09e-03	2.42e-03	0.831	1.75e-04
Mode 6	2.19e-04	1.10e-06	5.55e-07	1.33e-01	9.60e-03	0.949

TABLE 3.8 MAC table between 6 modes from EMA test and analytic solution, Case 4

	Out-of-plane mode			in-plane mode		
	Mode 1	Mode 2	Mode 3	Mode 4	Mode 5	Mode 6
Mode 1	0.981	9.03e-03	4.90e-03	1.25e-04	3.86e-03	1.06e-04
Mode 2	1.73e-03	0.890	2.60e-02	8.78e-05	5.01e-05	2.50e-05
Mode 3	3.62e-03	8.58e-03	0.886	1.67e-05	1.88e-05	8.41e-06
Mode 4	2.72e-05	7.35e-06	8.88e-07	0.997	1.63e-02	1.18e-02
Mode 5	4.84e-03	9.50e-05	9.62e-07	5.81e-04	0.986	3.77e-03
Mode 6	1.11e-05	1.44e-05	2.90e-05	1.76e-02	4.69e-03	0.985

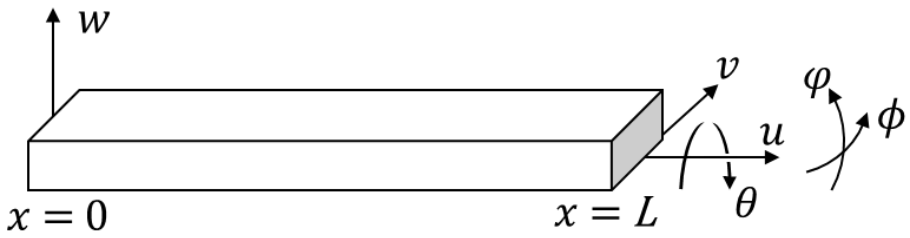

Figure 3.1 Coordinates of a beam component

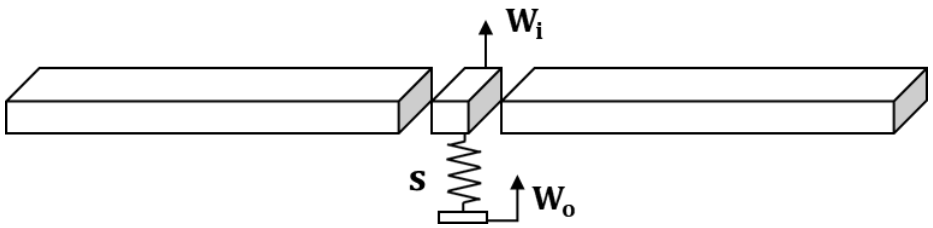

Figure 3.2 Diagram of an infinitesimal element of a beam component

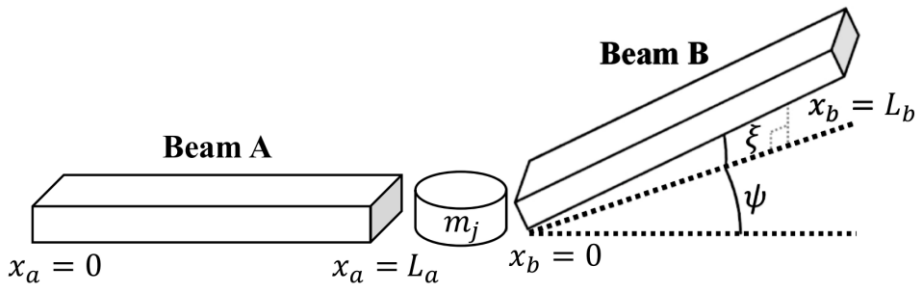

Figure 3.3 Rigid frame structure with an arbitrary coupled angle

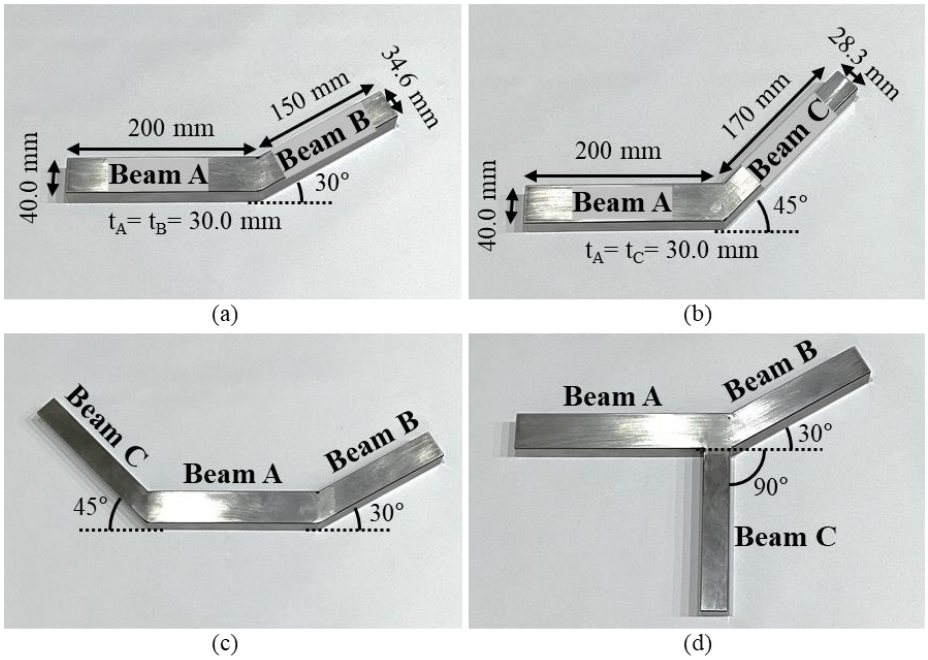

Figure 3.4 Four rigid frame models for verification. Case (a) 1, (b) 2, (c) 3, and (d) 4

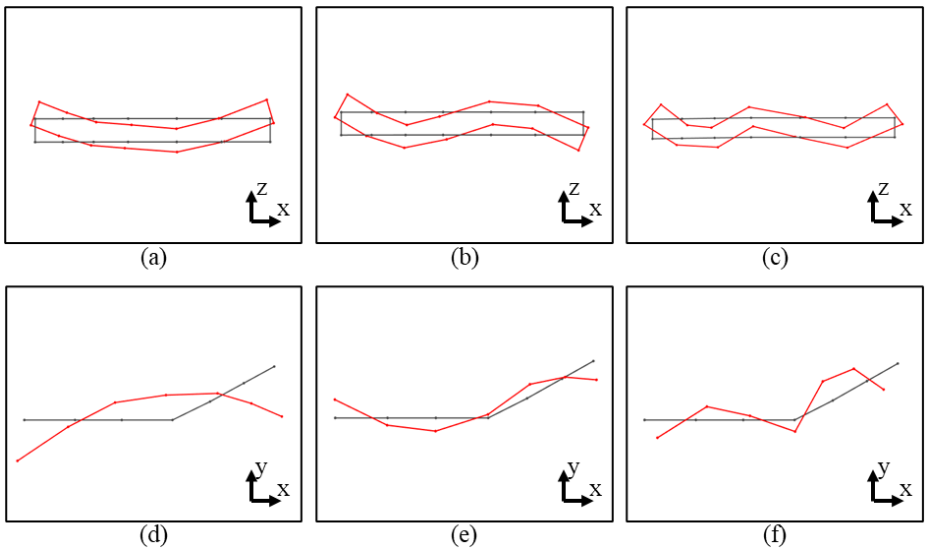

Figure 3.5 Mode shapes of two-beam coupled structure. First (a), second (b), and third (c) mode shape of out-of-plane vibration, and first (d), second (e), and third (f) mode shape of in-plane vibration

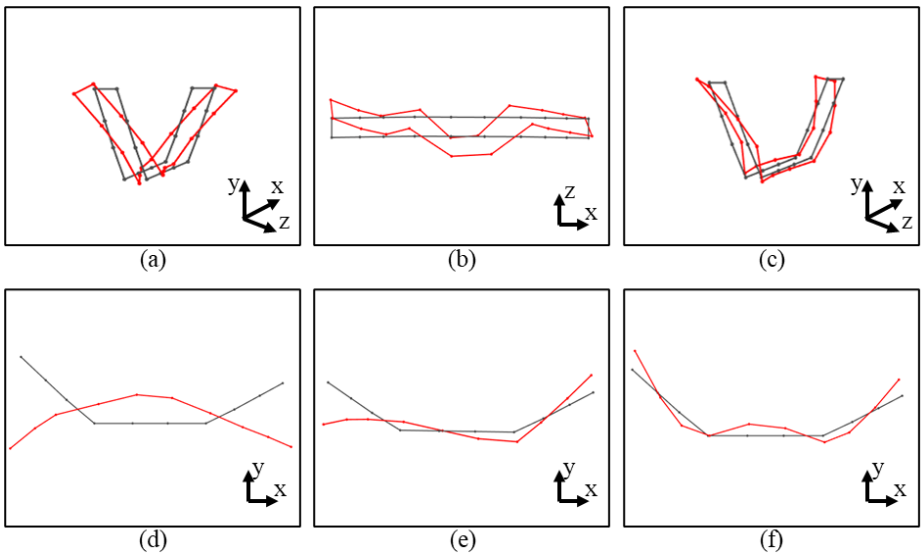

Figure 3.6 Mode shapes of Case 3. First (a), second (b), and third (c) mode shape of out-of-plane vibration, and first (d), second (e), and third (f) mode shape of in-plane vibration

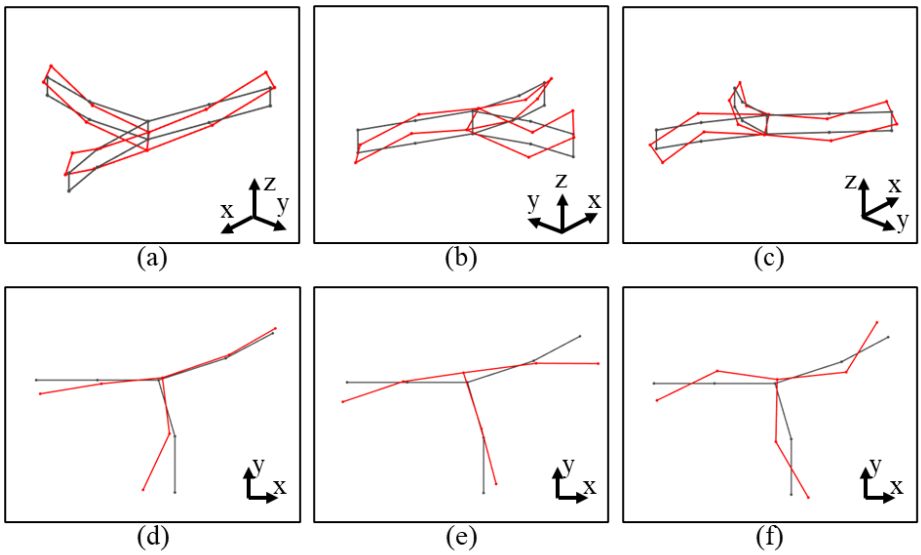

Figure 3.7 Mode shapes of Case 4. First (a), second (b), and third (c) mode shape of out-of-plane vibration, and first (d), second (e), and third (f) mode shape of in-plane vibration

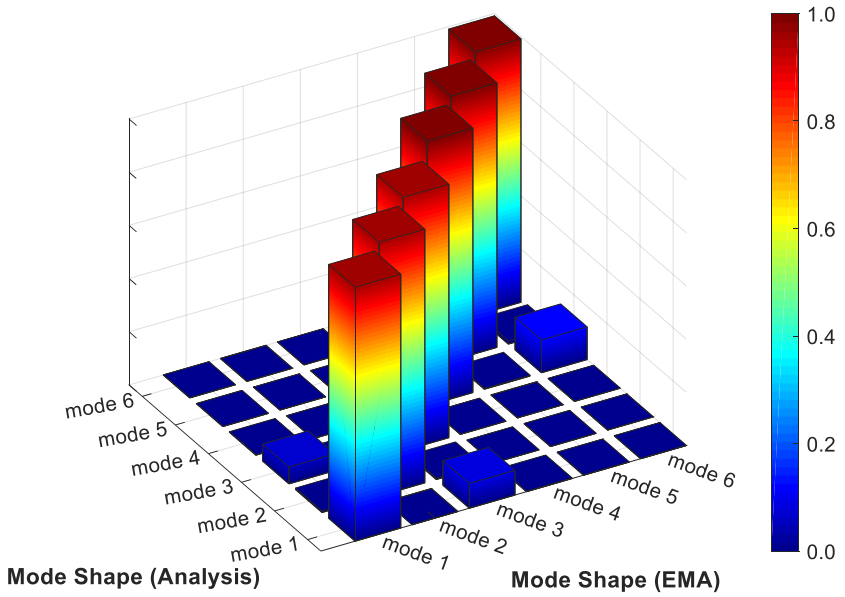

Figure 3.8 MAC matrix between 6 modes from EMA test and analytic solution, Case 1

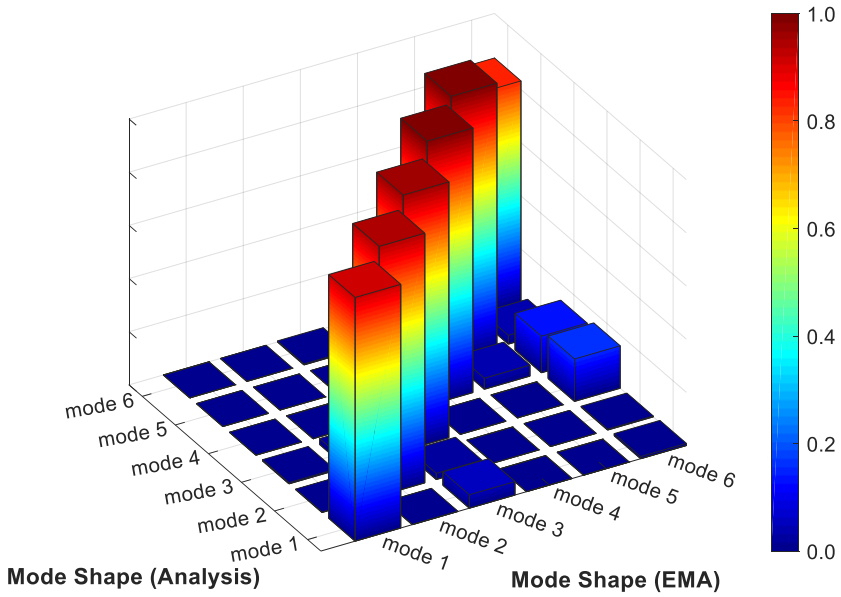

Figure 3.9 MAC matrix between 6 modes from EMA test and analytic solution, Case 2

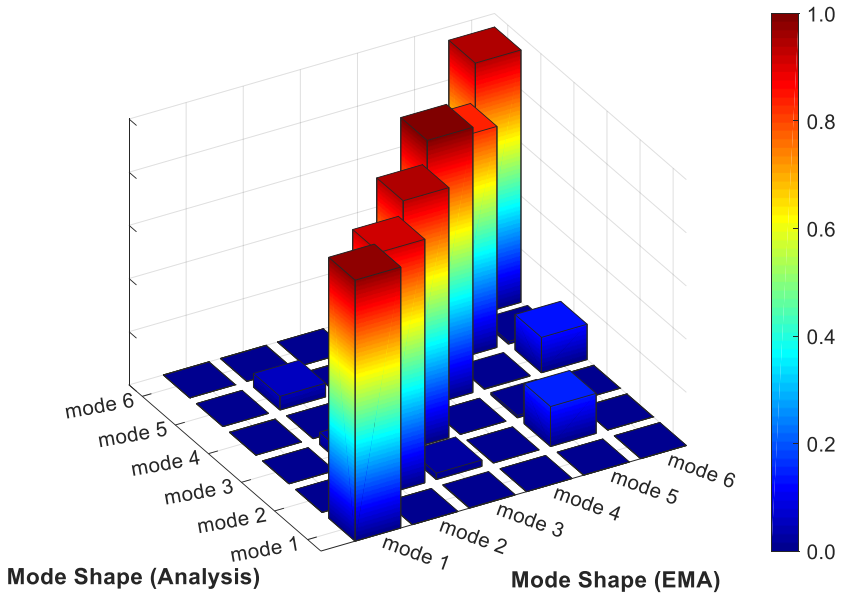

Figure 3.10 MAC matrix between 6 modes from EMA test and analytic solution, Case 3

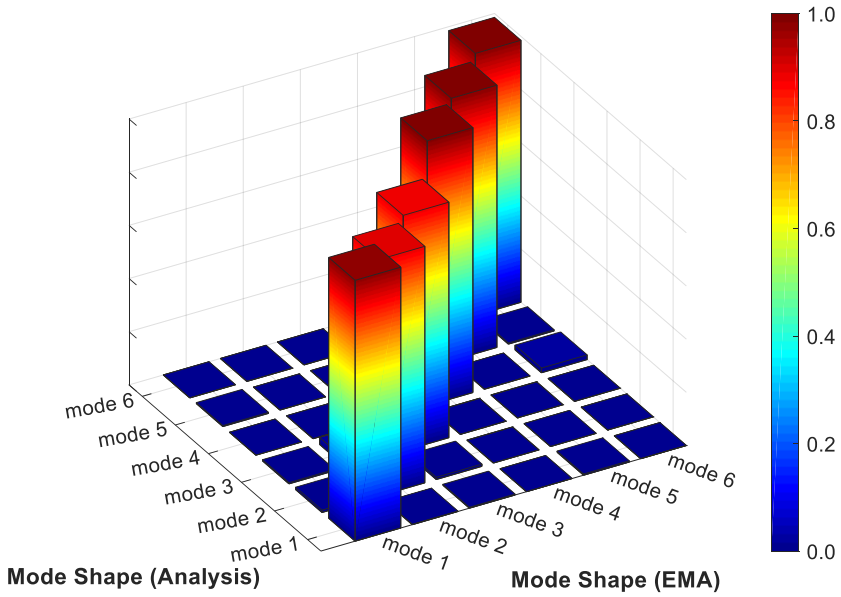

Figure 3.11 MAC matrix between 6 modes from EMA test and analytic solution, Case 4

CHAPTER 4

PREDICTION OF TRANSFER CHARACTERISTICS OF COMBINED STRUCTURE

4.1 Introduction

This chapter deals with the prediction of transfer characteristics of combined structure. As mentioned above, the dynamic property of the whole coupled system can be estimated by using predictive dynamic substructuring technique. In this study, one frame-shaped part of a vehicle suspension system is considered as one substructure, and the rest of the vehicle system are a separate subsystem. The transfer characteristics of the entire vehicle system and the separate subsystem which the frame-shaped part has been removed are experimentally measured, and the changes of the dynamic characteristics of frame-shaped substructure are theoretically analyzed by the linear algebraic formulation in chapter 3. These two characteristics are coupled applying the FBS method to estimate the dynamic characteristics of the combined system. For conventional FBS method, every changed model of the subcomponent is needed to be manufactured and tested to obtain the transfer characteristics. However, with the suggested predictive method, after conducting only a single

experimentation of the initial specification, it is possible to predict transfer characteristics of complete system without additional experiments for arbitrary modification of the subcomponent. At the end of this study, the FRF coupling process are verified by comparison between the predicted and the measured transfer characteristics.

4.2 Joint property identification

The basic concept and the theoretical formulation are described in chapter 2.2. To apply the dynamic substructuring technique, additional theoretical concepts for improving FBS method are introduced in this chapter: the identification of joint property. The concept of joint property, which was introduced by Mehrpouya [5], is the experimental estimation of the change of the transfer characteristics which representing the difference between joining methods of an ideal assumption and a practical assembly. As considering the assumption of one point coupling in Fig. 2.1, a welded coupling is well-matching with the assumption. However, for the assembly of complex system like a vehicle are not adopting the point welding but using a bolt coupling. Due to the convenience and the reversibility of coupling which enabling the replacement of components, the bolt coupling method is preferred for the practical assembly of the vehicle system. In this case, the characteristics of coupled system change because of the parameter change such as added bolt mass or stiffened interface. According to the research by Kim et al. [19], Eq. (2-6) are altered with the addition of a joint property.

$$\mathrm{H}_{O,I}^{\mathrm{AB}} = \mathrm{H}_{O,I}^{\mathrm{A}} - \mathrm{H}_{O,J}^{\mathrm{A}}\left(\mathrm{H}_{J,J}^{\mathrm{A}} + \mathrm{H}_{J,J}^{\mathrm{B}} + \mathrm{H}_{J}\right)^{-1}\mathrm{H}_{J,I}^{\mathrm{A}} \qquad (4\text{-}1)$$

As expressed in Eq. (4-1), the transfer characteristics of combined system, H^{AB}, can be computed with the FRFs of subsystems, H^{A} and H^{B}, and the joint property H_J as an equal format with FRFs. In other words, the joint property can be computed with the FRFs of the system following the Eq. (4-2).

$$\mathrm{H}_J = \mathrm{H}^{\mathrm{A}}_{J,I}\left(\mathrm{H}^{\mathrm{A}}_{O,I} - \mathrm{H}^{\mathrm{AB}}_{O,I}\right)^{-1}\mathrm{H}^{\mathrm{A}}_{O,J} - \mathrm{H}^{\mathrm{A}}_{J,J} - \mathrm{H}^{\mathrm{B}}_{J,J} \qquad (4\text{-}2)$$

Considering the joint property, only the dynamic characteristics of changed subsystem are required to be tested if the dynamic properties and the joint property of initial system have been measured. Furthermore, the theoretical FRF prediction of a changed subcomponent makes the additional experiment process unnecessary.

4.3 Experimental verification

Dynamic substructuring using predicted transfer characteristics of substructure was verified with a vehicle system. As shown in Fig. 4.1 a bent beam shaped component was selected as a frame-shaped subsystem, and it was replaced by a rigid frame structure which was made of aluminum. The frame structure was a two-beam coupled structure. The geometric features of two beam components are determined to have a shape to the original part of the vehicle system. Detailed shapes of two beam components which consist the frame-shaped substructure are listed as followed: equal thickness of 30 mm, width of 60 mm and 36 mm respectively, and length of 170 mm and 210 mm. The material information of the frame-shaped structure was listed as followed: Young's modulus of 69 KN·mm2, Poisson's ratio of 0.33, and volume mass density of 2705 kg·m3. Two beams are combined with 53 degrees of coupling angle. The FRFs of the frame structure were tested using the tri-axial accelerometers (356A15, PCB Piezotronic) and impact hammer (Type 8206-002, Brüel & Kjær).

The input position of this experimentation was defined as a wheel hub position which is generally considered as input point when researching the vehicle suspension system, and the output positions were defined as an interior

noise at the driver's left ear and vibrations at the seat and floor where contact directly to the human body.

To estimate the changes of the transfer characteristics of the vehicle system, dynamic properties of two subsystem and the joint property at the joining point of target component are required. The dynamic properties were obtained as the form of acceleration over force, called inertance FRF, using aforementioned sensors; tri-axial accelerometers and impact hammer. By using same bolt connection, the FRFs of the joint properties and the rest of vehicle system other than the target component were measured and can be used to predict the transfer characteristics of the entire system. Then, the dynamic characteristics of the changed component which was a rigid frame structure made of a couple of aluminum beam were predicted by solving a linear algebraic formulation $\mathbf{CA} = \mathbf{F}$ introduced in Eq. (3-39). The characteristic matrix $\mathbf{C}$ was determined as expressed in Eq. (3-40), and the force vector $\mathbf{F}$ was defined as a unit vector that one element is 1 and the others are all zeros. This force vector which consists of one and zeros are representing the definition of FRF: the response function about a unit force of all frequency range. The position of element 1 in the force vector can be inferred by considering the free boundary condition in Eq. (3-39). For instance, the force vector that has element 1 at first row and the others are all zeros means that a unit force of all frequency range is excited into

$x = 0$ location of the beam A, and the computed responses of the frame structure is equal to the FRF by the z-axis excitation at the same location.

Finally, the dynamic characteristics were predicted by combining the measured and analyzed FRFs of each subsystem based on the dynamic substructuring technique as following Eq. (4-1). In Fig. 4.2, the predicted transfer characteristics by predictive dynamic substructuring were compared with the measured signal by replacing the origin part with the rigid frame structure as shown in Fig. 4.1. Input P1–3 in Fig 4.2 represents the x, y and z axis input force at the wheel hub position, and Output P1–7 represents the sound pressure level on vehicle interior noise and each three axis vibrations at the seat and floor in order. In the prediction results, errors occurred in certain ranges, such as around 100-150Hz, and these errors are considered to be caused by reasons such as pre-load or nonlinearity in the bushing of removed parts. In addition, it can be confirmed that the prediction results in this study are very accurate compared to other studies. To verify the accuracy of proposed method, the Frequency Response Assurance Criterion (FRAC) in Eq. (4-3) were used to compare measured and predicted frequency response functions [40].

$$\mathrm{FRAC} = \frac{\left|\sum_{\omega=0}^{\omega_e} \mathrm{H}_1 \mathrm{H}_2^*\right|^2}{\left(\sum_{\omega=0}^{\omega_e} \mathrm{H}_1 \mathrm{H}_2^*\right)\left(\sum_{\omega=0}^{\omega_e} \mathrm{H}_2 \mathrm{H}_2^*\right)} \tag{4-3}$$

The FRAC value close to 1 represents that spectral characteristics of two FRFs are almost identical. Generally, this indicator should be above 0.8 to obtain the consistency of prediction [41]. FRAC The mean FRAC values between measured and predicted FRFs was computed considerably high as 0.82, therefore the prediction of transfer characteristics ensured its accuracy.

To compare the accuracy of the predictive dynamic substructuring and the conventional dynamic substructuring, transfer characteristics of the complete vehicle system were computed again using experimentally measured transfer characteristics of same subcomponents as shown in Fig. 4.3. Some of the graphs in Fig. 4.3 showed increased prediction accuracy, but most of them were confirmed to have higher error and additional peaks are generated, and the mean FRAC value was also reduced to 0.43. In this experimental verification, it is judged that such an error occurred due to the signal noise at the anti-peak frequencies and physical limitations such as twisting of the impact axis when measuring the FRFs of a sub-component. When performing the dynamic substructuring technique, the error or noise in transfer function causes significant error since matrix inversion is included in the calculating process. Therefore, the predictive method proposed in this study is more useful and can estimate the transfer characteristics of coupled systems with high accuracy.

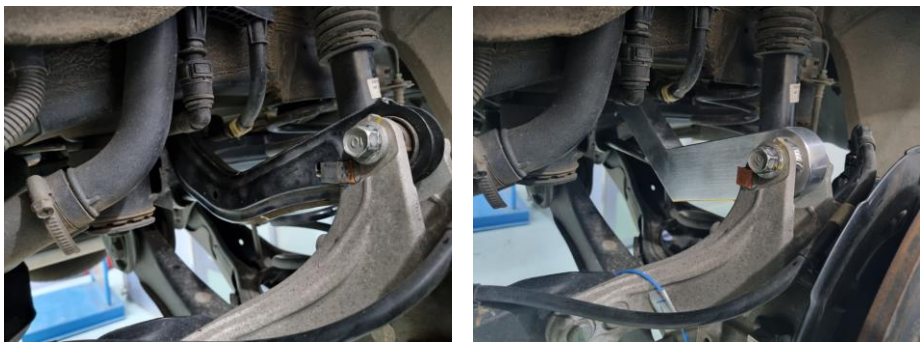

Figure 4.1 Target component of vehicle system (left) and the frame-shaped alternatives (right)

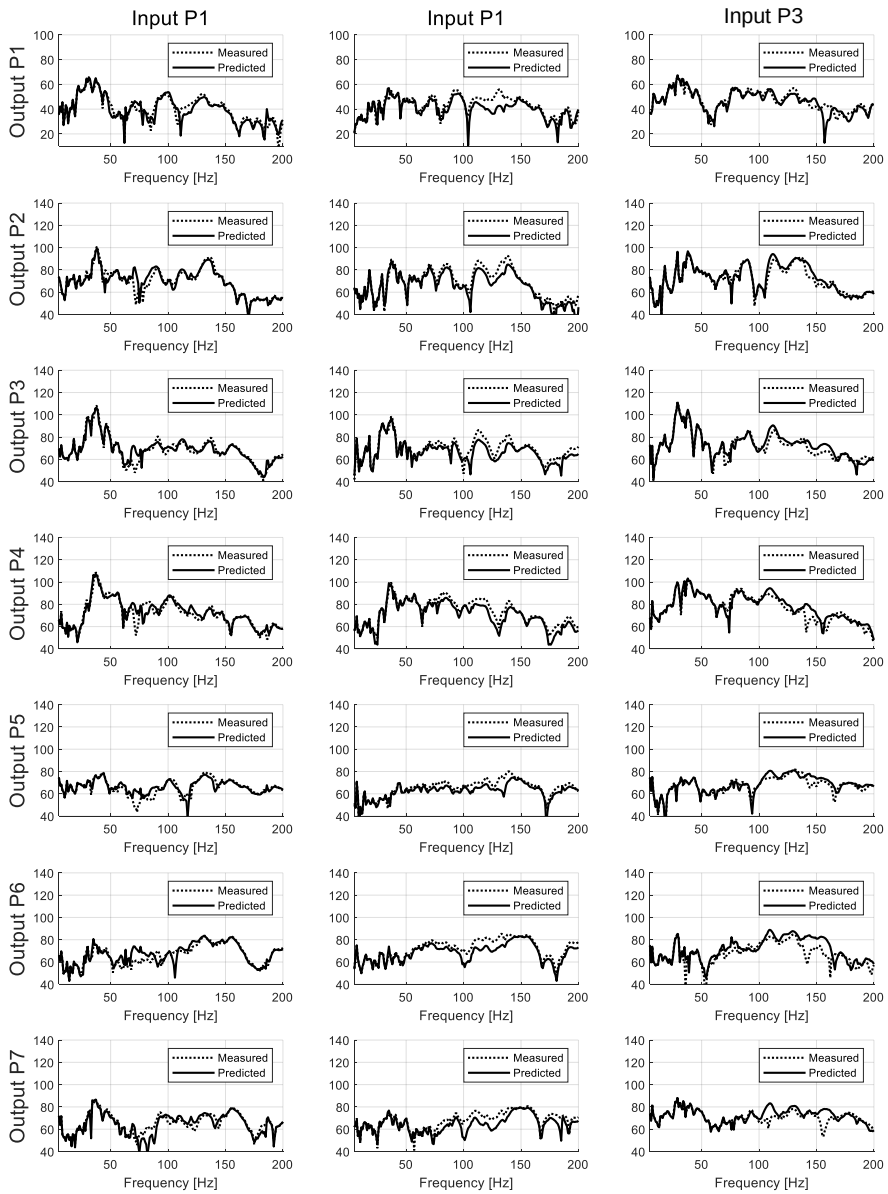

Figure 4.2 Predicted FRFs of the tested full vehicle system using predictive dynamic substructuring

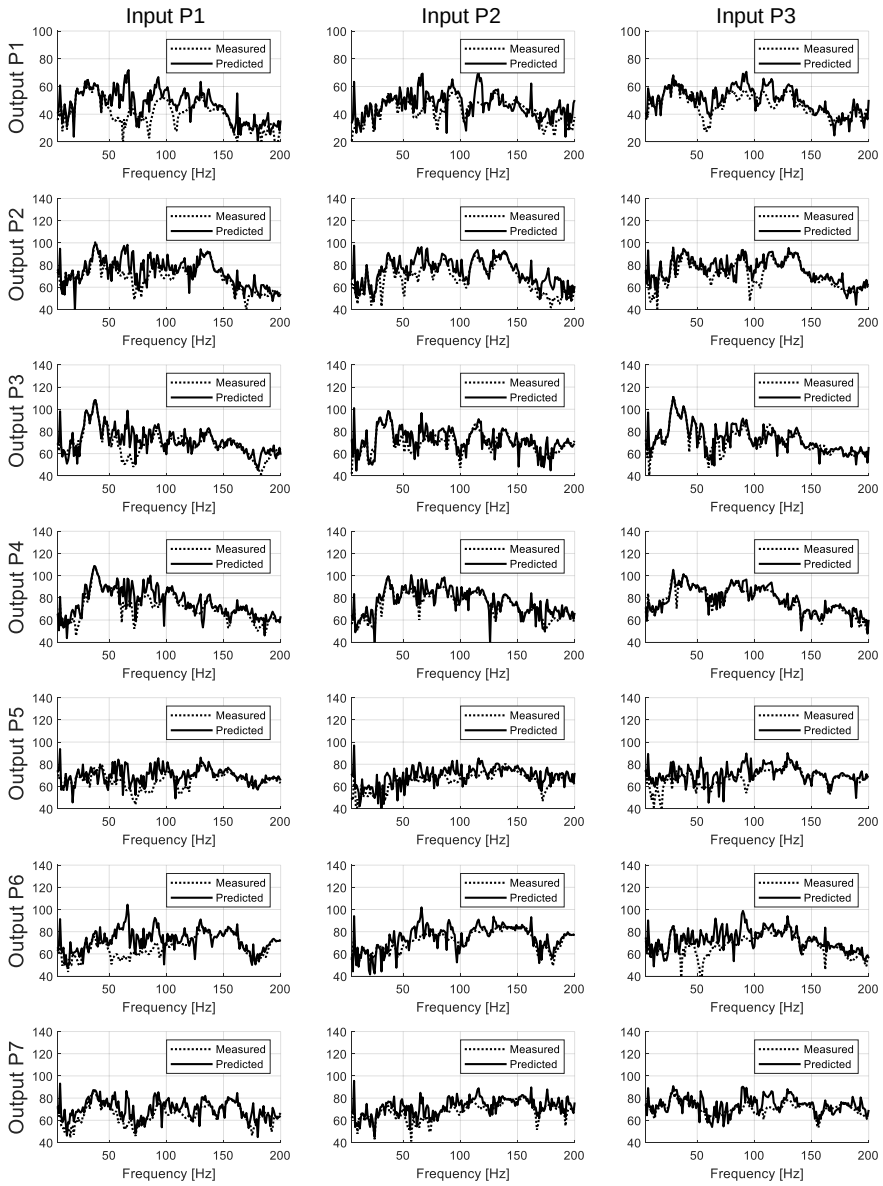

Figure 4.3 Predicted FRFs of the tested full vehicle system using conventional dynamic substructuring

CHAPTER 5

APPLICATION OF PREDICTIVE DYNAMIC SUBSTRUCTURING

5.1 Introduction

This chapter introduces two cases for using the proposed predictive dynamic substructuring. The first is to predict the noise and vibration generated in the driving test condition of the complete vehicle system that has been used for the verification of the predictive dynamic substructuring in chapter 4. Using the blocked force concept, the input force generated during driving is equivalently obtained, and the noise and vibration responses are calculated by multiplying this force acting on the input point with the transfer characteristics of the complete vehicle system which are previously obtained in chapter 4. As shown in Fig. 3.4, this process is applied to each of the 4 frame samples used for verification in chapter 3 to prove its practicality.

The second is to predict the change in subjective vehicle ride quality according to the change in the frame-shaped subcomponent. After analyzing the correlation between the measured vibration and the subjective evaluation score using statistical techniques, the change in vehicle ride quality according to the

change in the subcomponent is quantitatively predicted by combining the predicted vibration response using predictive dynamic substructuring. Similar to the prediction of vibratory responses, this application case uses the full vehicle system used in chapter 4 to confirm the practicality, and introduces the process of optimizing ride quality score through a parametric study of the change in the geometric information of the frame-shaped subcomponents

5.2 Prediction of dynamic responses

5.2.1 Blocked force

Similar to the transfer characteristics, the dynamic responses can be also predicted with the constant input force at the input position. However, the input force and the input point are considerably hard to define for various machinery system. The concept of blocked force is introduced to overcome this situation. As reviewed by Van der Seijs [13], The blocked force is the concept of a virtual force which is consistent regardless of the changes at the passive side. A combined system can be divided into two parts: passive and active side. The active side is a subsystem which contains the input point where the operational force is excited, and the passive side is the other subsystem which receives only the force transmitted from the opposite subsystem through the joint with no

external force applied. As depicted in Fig. 5.1, the blocked force is an equivalent force that replacing the input force at the input point with a virtual force applied at the joining point. The blocked force is used to substitute an input force which is hard to define the excitation point. For example, the road excitation throughout the wheel-tire system and internal combustion excitation in the engine cylinders are difficult to define the exact points of action, therefore these excitations are replaced with the joining positions such as wheel hubs and engine mounts respectively. The blocked force of the system can be obtained as follow:

$$\mathrm{H}_{O,J}^{\mathrm{B}}\left(\mathrm{H}_{J,J}^{\mathrm{A}}+\mathrm{H}_{J,J}^{\mathrm{B}}\right)^{-1}\mathrm{H}_{J,I}^{\mathrm{A}}f_I=\mathrm{H}_{O,J}^{\mathrm{B}}\left(\mathrm{H}_{J,J}^{\mathrm{A}}+\mathrm{H}_{J,J}^{\mathrm{B}}\right)^{-1}\mathrm{H}_{J,J}^{\mathrm{A}}f^{bl} \quad (5\text{-}1)$$

$$f^{bl}=\left(\mathrm{H}_{J,J}^{\mathrm{A}}\right)^{-1}\mathrm{H}_{J,I}^{\mathrm{A}}f_I. \quad (5\text{-}2)$$

As derived in Eq. (5-2), the blocked force is determined only with the dynamic properties in the active side. With these characteristics of blocked force, it is suitable to substitute the operational input force when considering the modification of the passive side subsystem.

5.2.2 Vibration and noise prediction

This test was performed to evaluate the vibrations which were transmitted to human body during road driving test. For this operational testing condition, output points of vibratory responses of the complete vehicle system were seat and floor which is the actual contact point between vehicle and driver's body, and practical input points were the contacting point of vehicle tires and the pavement which were identical to the case in chapter 4.3. However, due to the difficulty of measuring forces at the interface between the tire and the road surface, the input point was changed into a wheel hub position where the joining point of wheel-tire system and the rest of vehicle system using the concept of blocked force. The virtual equivalent force was measured instead of actual input forces so that vibratory responses of output position in vehicle system can be obtained by multiplying the blocked force and the transfer characteristics between the output position and wheel hub position. Another advantage of blocked force is the consistency for the change of passive system, the rest of vehicle except the wheel-tire system in this case. Thus, if changes of the transfer characteristics of the passive system were predicted, changes of the vibratory responses at the output position could be defined with the measured blocked force. As shown in Fig. 5.2, the predicted vibratory responses were matched well to the measured vibration signal. The mean absolute error between overall

level of the predicted and the measured vibration was computed as 1.08 dB (highest error level is 1.94 dB), and it is quite low level of error that barely perceptible to human body. For vehicle interior noise, identical process was applied to prediction for the change of subcomponent. The transfer function of noise level, called noise transfer function (NTF), were predicted as shown in chapter 4. The result of prediction was depicted in Fig. 5.3 and showed high accuracy similar to the prediction of the vibratory responses. The error between overall level of the predicted and the measured noise was 0.20 dB which is unnoticeable of human hearing.

5.2.3 Modification of subsystem

Using the predictive dynamic substructuring, the changes in the dynamic responses are simply computable for the change of the subcomponent. To ensure the usability of the proposed method, the prediction was made by replacing the above-mentioned component with the four frame-shaped structures which are the experimental verification samples, Cases 1–4, in chapter 3.3. The predicted vibrations and interior noise were computed for the substructure samples as shown in Fig 5.4 and 5.5, and the overall levels of noise and vibrations are listed in Table 5.1.

5.3 Prediction of vehicle ride quality

5.3.1 Evaluation of whole-body-vibration

This stage proposes the other application case that using the predictive dynamic substructuring for an experimental method to evaluate the perceptual feeling for the vehicle induced vibration in the case of vehicle ride quality. Technological research on NVH issues with vehicles typically consist of two parts: 1) Mechanical control to minimize undesirable NVH problems, and 2) cognitive improvement to heighten sensitivity to vibration and sound stimuli when driving a car. The values of the acceleration and sound pressure levels can be used to quickly evaluate the NVH difficulties of the earlier section. The latter part's perceptual issues, however, are challenging to quantify. Because to the lower reproducibility and higher complexity of the materials, vibratory perception—known as ride quality—cannot be quantified to the same extent as auditory sensitivity. Currently, in the automobile sector, evaluations of ride quality rely on the scores given by a select group of experts with considerable driving experience. Despite the specialists' rigorous training, this empirical review merely provides the comfort rankings of the target vehicles, which are easily altered by physical or psychological factors. Due to the inherent limitations of the traditional method, various institutes have explored quantitative assessment methods for vehicle comfort in detail.

To calculate the subjective comfort level from the recorded vibration signals, numerous research has been done. Using an electro-dynamic table, Miwa [42] investigated the equal feeling levels of translational vibration. Griffin [43] performed adjustment tests to see whether random vibrations in the tonal and octave bands were subjectively equivalent. Griffin and Whitham [44] investigated the link between lateral and vertical signals that cause comparable amounts of discomfort. In order to evaluate the level of discomfort caused by whole-body vibration (WBV) for translational and rotational oscillations, Parsons and Griffin [45] took into account combined-axis motions. Plotting equal feeling contours for WBVs of sinusoidal and random signals was done by Donat et al. [46] using the floating reference approach, which involves a specific presentation sequence of the test stimuli. In both lab and outdoor investigations, Mistrot et al. [47] performed discomfort evaluations. Also, the perceptive reaction to low-level vibration was investigated using the magnitude estimation method [48], and the vibration threshold for the wide range of frequency was researched using the adjustment method and signal detection [49]. Based on these research, the international ISO 2631-1 standard [50] for assessing WBV perceptions was created. This document describes the measuring and evaluation techniques for various vibration types. The vibrating axis and exposure location are said to affect the perceptual qualities of WBV,

according to the standard. To compute the levels of discomfort or perception from a combined WBV via subjective assessments, weighting and multiplying factors are provided. This approach was used in several research to assess different aspects of cognitive responses. For low frequency reference signals of 5 or 20 Hz, Morioka and Griffin [51] employed the up-and-down transformed response (UDTR) approach to identify noticable vibrational variations. In order to get around the overlapped scales in the ISO 2361-1 standard, Kaneko et al. [52] looked at explicit scales of comfort. The category judgment method was used to plan the subjective test using three types of stimuli with various spectral properties. For the sensationally equal dynamic responses and forces, Mansfield [53] employed a modified version of Bruceton test protocol, a modification of UDTR test, confirming the curves that had previously been shown. Nahvi et al. [54] examined the riding comfort of a sedan-type passenger vehicle. Using quantification criteria including the seat effective amplitude transmissibility (SEAT) values, international roughness index (IRI), and weighted values according to the international standard of ISO 2631, the recorded vibrations underwent a thorough analysis. An equation for WBV prediction in participants who seated in the postures of nonneutral position of head and neck was verified by Rahmatalla and DeShaw [55]. WBV was tested both subjectively and objectively by Kim et al. [56]. Mansfield and Maeda [57]

subjectively evaluated the link between the subjective scores and the observed vibration by the multiple regression of vibrations in multi-axis. Recently, utilizing the rating [58] and three-down one-up [59] procedures, a modified UDTR methods, subjective and objective testing were carried out and studied for a variety of seated postures. On patients in semi-supine positions, Govindan [60] tested and confirmed the exponential properties of vibration feeling. And Li [61] contrasted the vibration feeling of a hard and cushioned seat. In order to assess the comfort of vehicle vibration, Du et al. [62] built four models using a feedforward-type neural network and using gated recurrent units. The estimating accuracy of this standardized method is insufficient for use in earlier step of vehicle design, despite the fact that evaluation only using the weighted WBV is comfortable. A linear model has been used for advanced evaluation [56,60]. The analysis, however, took into account just a small number of WBV factors, and no other samples were used for validation. Furthermore, a significant amount of research has been done to assess the vibratory perception using a wide range of techniques, including the IRI index [63], ride number [64], and Sperling's index [65]. Unfortunately, these are difficult to apply when comparing the quality of a vehicle's ride because they are primarily applicable to pavement evaluation.

The purpose of this chapter was to provide a test-based methodology for reliable and precise vehicle comfort assessment. Based on driving tests using 6 sedan-style test vehicles, 17 test conditions, and objective vibration measurements, subjective jury evaluations, and other analyses were performed. Eleven jury members provided subjective evaluations, and the observed vibrations were then corrected using the weighting curves with the multiplying factors specified in ISO 2631-1. Principal component analysis (PCA) and multiple linear regression (MLR) were used to organize a precise quantification of subjective responses after statistical analysis of the results from both tests. According to the vibration's frequency range, primary ride and secondary rides were divided to classify vehicle-induced vibrations [66]. The primary ride takes into account low-frequency bodily motions, whereas the secondary ride takes into account higher-range vibration that feels trembling. Each category is connected to certain vehicle attributes. As a result, different strategies and corrections are needed for various vibration types. As a result, two models in the form of regression equations were independently developed for each type of vibration. The ride quality of automobiles could be accurately and robustly evaluated with solely the measured vibration of a specific vehicle using the indices and development methods in this work. Combining the secondary RQI model and the prediction of vibratory responses in chaper 5.2, the change of

vehicle ride quality can be predicted evaluated according to the change of subsystem.

The underlying theoretical principles are discussed in depth in earlier works and cited in the ISO 2631-1 and BS 6841 standards. The subject's postures were used to standardize the vibratory sensitivity. Fig. 5.6 shows the axes of the seated positions. Fig. 5.7 displays the weighting curves for the identical vibratory experiences. At frequencies where the weighting values were smaller, the perceptual qualities were less sensitive. The weighted vibration a_{w1} and the multiplying factor k_1 of each axis were used to merge the multi-axial vibrations as a single variable, as stated in Eq (5-1).

$$a_{total} = (k_1^2 a_{w1}^2 + k_2^2 a_{w2}^2 + \cdots + k_n^2 a_{wn}^2)^{1/2} \qquad (5\text{-}1)$$

Table 5.2 provides application guidelines for the weightings and factors used to measure perceived vibration and ride quality. This standard serves as the underlying premise for determining the overall magnitude of vehicle-induced vibrations, and the ISO 2631-1 standard states that low-frequency vibrations between 0.5 and 80 Hz have an impact on the seated posture. The WBV at the driver position is divided into primary and secondary rides, as mentioned in Section 1. The major ride factor takes into account the sprung

mass property of automotive suspension systems. The primary ride's frequency range was under 5 Hz. The secondary ride is associated with the unsprung mass feature of automobiles and quivering vibration which occurs at frequencies greater than 5 Hz. In general, the primary ride sense is influenced by the vehicle's global motion, and the drivers are bothered by the interface vibration of their seats or floors, called the secondary ride feeling. For these two kinds of vibrations, the calculation and summation of the vibration metrics and test of ride quality scores were carried out independently using the standards and findings of earlier investigations.

5.3.2 Development of RQI models

Six mass-produced automobiles were used in tests for the formulation and verification of indices in actual driving situations. Subjective and objective evaluations were carried out under the identical test conditions. Nine axes in Fig. 5.6 were used in the testing for the upright sitting position. Driving evaluations were conducted at the Korea Automobile Testing and Research Institute's test site (KATRI). For the vehicle comfort test, eight different types of test roads, including soft asphalt and bumpy roads, were used. As can be seen in Table 5.3, the test conditions were increased in accordance with the vehicle speed and the type of test road and divided into primary and secondary rides

depending on the intended vibration type, for the shape and purpose of the test roads.

Using triaxial piezoelectric accelerometers (Type 4524, Brüel & Kjaer), which operate in the frequency range of 0.25-3000 Hz, the test vehicles' vibrations and global motions were measured. Siemens' Simcenter SCADAS Mobile was used as the data acquisition system. For the purpose of the primary ride evaluation, the vehicle motions—which are the low-frequency vibrations—consist of four axis accelerations: angular (roll, pitch, and yaw) and vertical (bounce) motions [67]. A seat pad type accelerometer was used to monitor the translational motion (bounce) (356B41, PCB Piezotronics). Four accelerometers mounted on the vehicle body frame can be used to acquire the low-frequency angular motions without causing any damage. Gyro-type sensors are typically used to measure the rotational components of vehicle motions. In order to verify the effectiveness of the non-destructive method, the spectrum responses of three rotational motions—pitch rate at a speed bump, roll rate at a curve—that are measured using a gyro-type sensor and accelerometers are shown in Fig. 5.8. The rotational responses from the two different sensor types were quite similar, with low error rates for both the maximum and average values (below 3% and 5%, respectively). As handling performance, which was not of interest in this investigation, is connected to the

yaw motion, it was eliminated from this step. With the verification from this pre-test process, the non-destructive measurement for the target rotational motions was ensured its availability.

To verify that the vehicle tests could be replicated, all measurements were carried out three times. Using a variety of metrics, the spectral properties of the measured vibrations were computed and merged into the vibration levels. The standardized curves in Fig. 5.7 were used to weight the acceleration spectra of three motions (pitch, roll, and bounce). Several metrics, including peak frequency, peak amplitude, overall magnitude, and power, were computed for each dynamic response. Eqs. (5-2) and (5-3) were also used to calculate the vibration-dose-value (VDV) and root-mean-square (RMS) to quantify the overall levels of the physical quantities in the time-domain.

$$\mathrm{RMS} = \left(\frac{1}{T} \int_0^T a_w^2(t) \mathrm{d}t \right)^{1/2} \tag{5-2}$$

$$\mathrm{VDV} = \left(\int_0^T a_w^4(t) \mathrm{d}t \right)^{1/4} \tag{5-3}$$

The impact of peaks on the time-domain data was examined using the RMS and VDV metrics, which are standard in the ISO 2631-1 standard. In addition, statistical metrics, kurtosis and skewness were employed as to

quantify the signals' spectral distribution. For the primary ride evaluation, the vehicle motions were therefore translated into 24 metrics, which correspond to the aforementioned eight metrics for each of the roll, pitch, and bounce motions. The primary ride test conditions were used to test and calculate these metrics (Nos. 1–9 in Table 5.3).

On each vibrational axis for the upright seated posture, the weighted acceleration's higher frequency range was quantified. The tri-axis vibrations of the seat and floor, which are in actual touch with the driver's body, were chosen to quantify secondary vibration. Similar to how the primary ride evaluation was conducted, the measured and weighted signals of all six axis were converted into RMS and VDV measurements. To add more information, summed values of each tri-axial vibration of the seat or floor, and the total merged values of all six axes were included in the quantification metrics. Referring the work by Bennur et al. [68], the harshness metrics for the vibration in the higher frequency range above 20 Hz were calculated for each axis and the merged values. Finally, 27 metrics from the measured vibration were calculated as the quantitative metrics for the secondary ride evaluation, nine metrics (six translational axes, two combined values for the seat and floor, and total merging value) were calculated for each of the RMS, VDV, and harshness. These

measurements were also conducted at the secondary ride test conditions (Nos. 10–17 in Table 5.3).

To rate each vehicle's ride quality, a subjective evaluation was performed. Regarding the study of Otto et al. [69], 11 skilled subjects were employed. The subjects gave scores for each vehicle sample at the same moment during the driving test with objective measurements. The participants were free of physical disorders and had the following anthropometric information: a mean age of 28.82 years (with a standard deviation of 2.72 years), a mean height of 177.82 cm (with a standard deviation of 5.28 cm), and a mean weight of 75.91 kg (standard deviation of 14.89 kg). According to Kolich's research [70], these physical characteristics have no relation to the comfort of the transmitted vibration, and since this study is not about individual cognitive characteristics, but about the average riding comfort people feel, there is no limit to the anthropological characteristics of the participants. The seven-point Likert scale, which went from extremely bad (Score 1) to extremely good (Score 7), was used to apply the category scaling method (Score 7). Also, while driving in the test conditions, the participants were instructed to score the ride quality of the car. To compare all test vehicles under all test situations, subjective evaluations were done. The sequence of the test vehicles and conditions was presented to each participant at random to prevent bias in the test procedure order. Subjects

first experienced each vehicle in the given order of vehicles for instruction purposes without ranking procedure. To guarantee the validity of the replies, the test was repeated at least three times. The assessed scores were divided by the geometric mean of the vehicle variation to normalize the ride quality score [57]. The assessed and normalized scores for all test conditions are listed in Tables 5.4 and 5.5. Simultaneously, the average and standard derivation of scores for each vibration type are depicted in Figs. 5.9 and 5.10.

In a multivariate statistical investigation with a large number of variables, PCA is a suitable way to reduce down the number of variables and identify the smallest set of underlying components that accurately reflects the whole distribution of the observed variables [71]. To simplify the test conditions in this investigation, PCA was used. The PCA analysis was performed on the score sets in Tables 5.4 and 5.5. The oblimin rotation algorithm was employed to rotate the factors since the ride quality scores of various testing conditions were thought to be interdependent. According to Table 5.6, exploratory factors for subjective scores were computed for each type of vibration. Each factor's degree of explanation for the score distribution is indicated by its eigenvalue. Three factors were taken into account to explain more than 97% of the information in each distribution of the primary and secondary ride ratings. Based on the correlation coefficients between the extracted factors and

tested scores, three test conditions for each vibration type were identified as being significant from the eigenvalues and factors. Given that the subjective ratings of Test conditions 6, 7, and 9 in Table 5.3 had the best correlation coefficients with the three factors, these conditions were chosen as the major conditions for the primary ride. Test conditions 10, 12, and 17 were similarly chosen for the secondary ride. Using IBM SPSS Statistics 25, the operations for this multivariate statistical analysis were conducted.

The ride quality index (RQI) models for each vibration type were developed according to the results of the MLR analysis between the evaluated scores and measured vibrations by also using IBM SPSS Statistics 25. The correlation equation (Eq. (5-4)), which is made up of a dependent variable $\hat{y}$, regression coefficients α_n, and multiple independent variables x_n, is defined using the MLR analysis technique [72]. The ordinary least squares method, denoted by Eq. (5-5), was used to minimize the square sum of error SE between the observed y_i and estimated $\hat{y}_i$ variables in order to estimate the coefficients and choose the variables.

$$\hat{y} = \alpha_0 + \sum \alpha_n x_n \tag{5-4}$$

$$\min_{\mathrm{SE}\in\mathbb{R}} \left\{ \mathrm{SE} = \sum (y_i - \hat{y}_i)^2 \right\} \tag{5-5}$$

The measured metrics under six major test conditions (three conditions for the primary and secondary rides, respectively) were employed as independent variables based on the results of the aforementioned exploratory analysis, and the normalized evaluation scores were used as dependent variables. The signals obtained under the six test conditions were used to calculate the vibratory metrics, which were discussed above. The scores and derived metrics were transformed logarithmically prior to the MLR analysis in accordance with Stevens' power law [73] which describes that the relationship between the intensities of the stimuli ϕ and human perception ψ are exponentially connected with the exponent β and constant k, as shown by Eq. 5.6 and 5.7. As a result, the variables included for the linear regression analysis were converted as the logarithmic values of stimulus level and perception level.

$$\psi = k\phi^{\beta} \tag{5-6}$$

$$\log\psi = \log k + \beta \log\phi \tag{5-7}$$

In order to ascertain the relationship with the subjective scores, the logarithm of the averaged scores were employed as dependent variable, and 153 metrics (24 and 27 metrics for each of the three road conditions of the primary and secondary rides, respectively) were included as independent variables. The

RQI models for the primary and secondary rides were developed as Eqs. (5-8) and (5-9) based on the MLR analysis [74].

$$\mathrm{RQ}_{\mathrm{primary}} = \alpha_{p0} + \alpha_{p1}x_{p1} + \alpha_{p2}x_{p2} \quad (5\text{-}8)$$

$$\mathrm{RQ}_{\mathrm{secondary}} = \alpha_{s0} + \alpha_{s1}x_{s1} + \alpha_{s2}x_{s2} + \alpha_{s3}x_{s3} \quad (5\text{-}9)$$

Table 5.7 lists the number of variables in each regression model, together with the constants α_{p0}, α_{s0} and the coefficients α_{pi}, α_{si} that were mated for each variable. The peak amplitude of the bounce motion under Test condition 6, x_{p1}, and the overall RMS value of the roll motion under Test condition 7, x_{p2}, are the two variables that consists of the primary-ride RQI. This model suggests that Test conditions 6 and 7 are the only conditions under which a vehicle's primary ride quality can be assessed. In the same way, three variables were adopted to construct the secondary-ride RQI model: the overall RMS values of the whole body vibration under Test condition 12, x_{s1}, the vibration of the feet under Test condition 17, x_{s2} and the harshness vibration under Test condition 10, x_{s3}.

Straight inference from the developed model revealed that the peak amplitude of the bounce motion and the overall level of the roll motion had a negative effect on the perceived primary ride quality. However, this

doesn't mean that there is no relation between the primary ride quality and the pitch motion. A vehicle improvement for reducing the target motion such as the bounce and roll motions also affect the overall characteristics of the sprung mass, including pitch motion. Consequently, the primary ride quality varies as a result of the applied modification, and it can be assessed using the primary RQI model. Furthermore, the RQI model's standardized coefficients offer a valuable insight that to improve the ride quality of vehicles the management of bounce motion has a significant impact on ride quality than roll motion. Similar to the primary ride RQI model, the secondary ride RQI model was employed to rate the score of secondary ride quality level of an unsprung mass vibration which was perceived by subjects, and it also imply how each vibratory metric contributed to the secondary ride quality.

To ensure the probabilistic dependability of the constructed MLR models, the statistical indicators were calculated simultaneously, as shown in Table 5.8. The high adjusted R-square values (Adj. R^2) obtained for the primary- and secondary-ride RQIs, which are close to 1, show the high accuracy of the developed model. And according to Fisher [75], the two models were proven to have statistical significance because their analysis of variance (ANOVA) p-values were less than 5%. With Durbin-Watson values between 1 and 3 [76] and variance inflation factors (VIF) smaller than 5 [77], the independence of

residuals and explanatory variables was verified for both RQI models. Also, the mean absolute percentage error (MAPE) between the observed and estimated scores by both models showed low error rates of 3.406% and 0.734%, respectively. These computed indicators statistically validated the two developed models' reliability.

5.3.3 Model verification

In the subjective evaluation process, the subjective scores of test samples were determined by comprehensively considering the variation of test vehicles and the chosen testing methodology. Since the variation and mean of the scores change based on the configured set of test samples, it is challenging to verify the availability of the designed index. Hence, the standardized scores of the vehicle ride quality, which were evaluated using various vehicle samples, were used to verify the proposed RQI models. Three sedan-style vehicles made up the sample set, and the testing procedures in chapter 5.3.2 was used to quantify the vibration measurements objectively. Unlike the initial inspection, a verification experiment was carried out on the specified road conditions, which were selected in the RQI variables, namely Test conditions 6, 7, 10, 12, and 17. In the index formulation phase, objective and subjective evaluations were performed under the same test settings. However, during the model

verification phase, the subjective assessment of the vehicle ride quality was tested using different subjects and test environments to verify the adaptability of the RQI models. The test roads for verification were arranged similarly to the KATRI test site in chapter 5.3.2 and were located in Iksan plant of Mando Corporation. The secondary ride test was undertaken on local public roads, including soft asphalt and uneven concrete pavements, while the primary ride test was carried out on a wavy test road for longwave and twist testing.

Six well-trained and physically healthy juries with a mean age of 44.17 years (standard deviation of 8.67 years old), a mean height of 174.33 cm (standard deviation of 3.50 cm) and a mean mass of 77.83 kg (standard deviation of 5.87 kg) evaluated the subjective ride quality of three test samples. As shown in Table 5.9, the ride quality scores obtained from the jury test and RQI estimation were separately standardized. As a result of verification procedure, the estimated ride quality scores showed low error rates and identical ranking orders for both developed models: 6.40% (MAPE) for the primary ride and 5.28% (MAPE) for the secondary ride. Through this verification process, both developed RQI models were confirmed their validity and the applicability of the experimental method for evaluation of vehicle ride quality were verified.

5.3.4 Ride quality prediction

Using the developed RQI models, the ride quality score can be estimated without additional experiment to measure the vibration signal transmitted to the human body. In this step, the prediction of secondary ride quality was conducted, and the primary ride quality was not aimed due to the generation of excitation were difficult at the extremely low ranges of frequencies for the primary ride quality. The transfer characteristics of complete vehicle system was predicted with the predictive dynamic substructuring suggested in this study, and the vibration signals were obtained for the human contact points with the operational blocked force in driving test conditions referred in chapter 5.3.2. For the sample target cases in 4.3, the ride quality scores were computed and observed to be improved from the 1.18 (original part) to 1.25 (changed part). Considering that the standard deviation of the evaluated ride quality scores in Fig. 5.10 is 0.11, the increase of 0.07 points indicates that there is a significant change in the transfer characteristics of the complete vehicle system even if one of subcomponents is changed.

Finally, based on these changes, a parametric study was conducted to find the direction of modification of the subcomponent to enhance vehicle ride quality. This was to change the geometric parameters of the identical subcomponent used in chapter 4. As shown on the right side of Fig. 4.1, and

this subcomponent was shaped of combined two beam elements: beam A which is close to the wheel hub and beam B on the opposite side. The four parameters, which were the thickness and the width of the two beam elements constituting the target subcomponent, were increased or decreased by +30% to -30%, and the change in vehicle ride quality due to the change in the design variable of the subcomponent was predicted using the predictive dynamic substructuring. In order to see the effect of the two beam elements separately, they are shown in Figs. 5.11 and 5.12, respectively, and the entire results of the prediction was organized in Table 5.10.

According to the results of prediction, the ride quality score of target vehicle was increased by increasing the thickness and width of beam element A. However, for design parameters of beam element B, score was the greatest when the increase in thickness and the increase in width were in an inverse relationship. In this parametric study, the predicted ride quality score showed the highest when thickness and width of beam element A increased as +30%, thickness of beam element B increased as +30% and width of beam element B decreased as -30%. In this way, using predictive dynamic substructuring, the analysis of all 625 cases in Table 5.10 can be performed in less than half an hour, and it is possible to perform predictions on a large number of cases

according to adopted parameters without manufacturing and testing of the subcomponent.

5.4 Result and discussion

In this chapter, two application cases using the predictive dynamic substructuring were introduced. First was the prediction of dynamic responses for the full vehicle system. To overcome the challenge of identifying the input force and the input location for mechanical systems, the concept of a blocked force was presented. The blocked force is equal to applying a virtual force at the connecting point in place of the input force at the input location. When predicting the changes on the passive side subsystem, the blocked force can be substituted for the operational input force because it can only be determined by the dynamic properties on the active side. Therefore, to measure the vibration responses of the output position in the vehicle system, the virtual equivalent force rather than the real input forces was measured. The prediction of vibratory responses was performed to assess the noise and vibrations that were transmitted to the human body when driving test was performed. Seat and floor were defined as output locations of the vibratory responses, while tires and pavement were defined as their input points. Similarly, vehicle interior noise at the driver's ear position was defined as output of auditory responses. With a low mean error of the vibration levels, the predicted vibratory responses closely matched the vibration signal that was actually measured. The same procedure was used to predict interior vehicle noise and the accuracy was ensured with

the low error level of overall sound pressure level. The subsystem was altered by swapping out the element with four structures in the shape of frames, which were same with the verification samples in previous chapter. The vibrations and internal noise levels were calculated easily for the frame-shaped substructures using the predictive dynamic substructuring proposed in this study.

For other application, vehicle ride quality, which is the subjective perception for the transmitted vibration was calculated using the proposed method and RQI models. The experimental evaluation models were designed in this work to assess the vehicle ride quality. Initially, primary and secondary rides were employed to separate the human perception of vibration. The low correlation coefficient (0.087) between the average scores of the two types of vibrations presented in Tables 5.4 and 5.5 indicates that each vibration type produced a different sensation in the human body. Under 17 different test conditions, subjective ride quality was evaluated for both vibration types. Six test conditions—three for the primary and secondary rides—were chosen using PCA as the major test conditions following the jury evaluation of the vehicle ride quality. The MLR analysis was used to relate the evaluated scores and measured vibration of the chosen conditions, and the RQI models for the two types of vibration were formulated. In this investigation, statistical indicators were used to ensure the probabilistic reliability of the

proposed RQI models. Finally, verifications of RQI models were performed by evaluating different samples with different evaluators, and the validity of the models was ensured with a low error rate. The designed evaluation model has the benefit of providing accurate and stable results for the assessment of vehicle ride quality. The evaluation outcomes of conventional methods rely on the subjective perception of a small number of juries which is influenced by the physical and mental conditions of the involved evaluators. The proposed models, on the other hand, offer a slight variation in evaluated ride quality score because they are based on measured vibration data. The ability to find directions to improve the ride quality of vehicles is another benefit of RQI models. The primary and secondary ride quality can be improved by reducing the chosen vibration metrics based on their interactions with the ride quality which were revealed using the MLR analysis as discussed in chapter 5.3. Without performing additional experiments, the ride quality score was estimated using RQI models. Predictive dynamic substructuring was used to predict the transmitted vibrations and the secondary ride quality score was computed from the vibration signal. To obtain an insight for improving the ride quality of the vehicle, parametric research was done to determine how the subcomponent should be modified. To predict how the design variable of the subcomponent would vary as a result of changes in the ride quality of the vehicle, the predictive

method suggested in this work was used. This parametric demonstrated that how to modify the shapes of each beam element to improve the ride quality of vehicle. This parametric optimization was useful since the parameters are not limited and rapid calculation is possible.

TABLE 5.1 Overall levels of the predicted vibrations and interior noise at the output position for Cases 1–4

Output position		Case 1	Case 2	Case 3	Case 4
Noise [dBA ref 2e-5]	Interior	67.28	67.75	68.27	69.12
Vibration [dB ref 1e-6]	Seat:X	124.06	126.27	125.38	124.36
	Seat:Y	135.98	137.05	138.19	135.40
	Seat:Z	132.13	135.00	133.16	134.07
	Floor:X	112.93	114.83	113.51	113.04
	Floor:Y	115.83	115.67	116.20	116.19
	Floor:Z	118.52	119.77	119.63	118.45

TABLE 5.2 Weighting curves and multiplying factors for the vibration perception of the seated posture

Coordinates	Axis	Weighting Curve	Multiplying factor
Seat	x-axis	W_d	1
	y-axis	W_d	1
	z-axis	W_k	1
Feet	x-axis	W_k	0.25
	y-axis	W_k	0.25
	z-axis	W_k	0.4
Rotation	Roll	W_e	0.63 [m/rad]
	Pitch	W_e	0.4 [m/rad]
	Yaw	W_e	0.2 [m/rad]

TABLE 5.3 Test conditions for the driving experiments

No.	Road name	Speed	Vibration type	Remarks
1	Speed bump	30 kph	Primary ride	All wheels bumped
2	Speed bump	35 kph	Primary ride	All wheels bumped
3	Speed bump	40 kph	Primary ride	All wheels bumped
4	Speed bump	35 kph	Primary ride	Single-side wheel bumped
5	Negative bump	35 kph	Primary ride	Square-shaped negative bump
6	Long-wave	60 kph	Primary ride	
7	Twist	60 kph	Primary ride	
8	Washboard	20 kph	Primary ride	
9	Corrugation	20 kph	Primary ride	
10	Highway	80 kph	Secondary ride	Asphalt
11	Highway	90 kph	Secondary ride	Asphalt
12	Highway	100 kph	Secondary ride	Asphalt
13	Highway	120 kph	Secondary ride	Asphalt
14	Highway	150 kph	Secondary ride	Asphalt
15	Rumble strip	50 kph	Secondary ride	Concrete
16	Rumble strip	65 kph	Secondary ride	Concrete
17	Rumble strip	80 kph	Secondary ride	Concrete

TABLE 5.4 Normalized scores of ride quality of test vehicle for the primary ride test

Test condition No.	Vehicle					
	A	B	C	D	E	F
1	0.858	0.835	1.369	1.160	1.263	0.696
2	0.843	0.730	1.489	1.348	1.236	0.655
3	0.729	0.634	1.744	1.490	1.545	0.539
4	0.988	0.796	1.289	1.152	1.125	0.762
5	0.985	0.739	1.280	1.182	1.231	0.739
6	0.826	0.978	1.154	1.154	1.017	0.913
7	0.998	1.074	1.653	1.559	0.967	0.374
8	1.061	0.925	1.360	1.278	0.925	0.635
9	0.892	0.730	1.298	1.292	1.027	0.892

TABLE 5.5 Normalized scores of ride quality of test vehicle for the secondary ride test

Test conditionNo.	Vehicle					
	A	B	C	D	E	F
10	0.981	0.918	0.981	0.949	1.076	1.108
11	0.799	0.876	0.979	0.959	1.332	1.142
12	0.971	1.058	0.842	0.907	1.230	1.036
13	0.895	0.895	0.970	0.858	1.342	1.119
14	0.928	0.787	0.886	0.935	1.265	1.307
15	0.782	0.869	1.035	1.201	1.242	0.952
16	0.914	0.987	0.914	1.060	1.206	0.950
17	0.869	1.024	1.055	1.117	1.055	0.905

TABLE 5.6 Total variance of distributions of ride quality scores for the two vibration types

Vibration type	Factor	Eigenvalue		
		Absolute	Variance [%]	Cumulative [%]
Primary ride	1	7.810	86.776	86.776
	2	0.593	6.591	93.367
	3	0.382	4.250	97.617
	4	0.203	2.257	99.874
	5	0.011	0.126	100.000
Secondary ride	1	4.928	61.596	61.596
	2	2.136	26.698	88.294
	3	0.744	9.305	97.599
	4	0.149	1.868	99.467
	5	0.043	0.533	100.000

TABLE 5.7 Variables and coefficients of the designed RQI models

Model	Variable	Unstandardized coefficient		Standardized coefficient
		Coefficient	Standard error	
Primary RQI	Const.	-3.241	0.624	-
	x_{p1}	-1.055	0.171	-0.709
	x_{p2}	-0.106	0.029	-0.421
Secondary RQI	Const.	-32.391	4.962	-
	x_{s1}	-0.809	0.032	-0.878
	x_{s2}	0.318	0.030	0.350
	x_{s3}	-0.191	0.065	-0.107

TABLE 5.8 Statistical indicators of the designed RQI models

Model	Adj. R^2	p-value (ANOVA)	Durbin–Watson	VIF	MAPE
Primary RQI	0.950	0.005	1.256	< 1.308	3.406 %
Secondary RQI	0.997	0.002	2.804	< 2.382	0.734 %

TABLE 5.9 Standardized scores of subjective evaluation test and RQI for verification procedure

Model	Vehicle	Subjective score	RQI estimation
Primary RQI	G	1.045	0.949
	H	0.854	0.898
	I	1.120	1.173
Secondary RQI	G	0.905	0.863
	H	1.176	1.143
	I	0.937	1.013

TABLE 5.10 Ride quality scores for the change of the design parameter (T_k: thickness of Beam k, W_k: width of Beam k)

			T_b																								
			-30%					-15%					0% (unchanged)					+15%					+30%				
			W_b																								
			-30%	-15%	0%	+15%	+30%	-30%	-15%	0%	+15%	+30%	-30%	-15%	0%	+15%	+30%	-30%	-15%	0%	+15%	+30%	-30%	-15%	0%	+15%	+30%
		-30%	1.177	1.212	1.229	1.239	1.245	1.212	1.232	1.242	1.247	1.249	1.229	1.242	1.248	1.249	1.249	1.239	1.247	1.249	1.249	1.248	1.245	1.249	1.249	1.248	1.247
		-15%	1.188	1.219	1.234	1.243	1.247	1.219	1.236	1.245	1.249	1.250	1.234	1.245	1.249	1.250	1.249	1.243	1.249	1.250	1.249	1.248	1.247	1.250	1.249	1.248	1.247
	-30%	0%	1.196	1.224	1.238	1.245	1.249	1.224	1.240	1.247	1.250	1.250	1.238	1.247	1.250	1.250	1.249	1.245	1.250	1.250	1.249	1.248	1.249	1.250	1.249	1.248	1.247
		+15%	1.202	1.228	1.241	1.247	1.250	1.227	1.242	1.249	1.251	1.251	1.240	1.249	1.251	1.250	1.249	1.247	1.251	1.250	1.249	1.248	1.250	1.251	1.249	1.248	1.247
		+30%	1.207	1.231	1.243	1.249	1.251	1.230	1.244	1.250	1.252	1.251	1.242	1.250	1.252	1.251	1.250	1.249	1.252	1.251	1.249	1.248	1.251	1.251	1.250	1.248	1.246
		-30%	1.188	1.219	1.234	1.243	1.248	1.219	1.237	1.245	1.249	1.250	1.234	1.245	1.250	1.250	1.249	1.243	1.249	1.250	1.249	1.248	1.248	1.250	1.249	1.248	1.247
		-15%	1.197	1.225	1.239	1.246	1.250	1.225	1.241	1.248	1.251	1.251	1.238	1.248	1.251	1.250	1.249	1.246	1.251	1.250	1.249	1.248	1.250	1.251	1.249	1.248	1.247
	-15%	0%	1.204	1.229	1.242	1.248	1.251	1.229	1.244	1.250	1.252	1.251	1.242	1.250	1.252	1.251	1.250	1.248	1.252	1.251	1.250	1.248	1.251	1.251	1.250	1.249	1.247
		+15%	1.210	1.232	1.244	1.250	1.252	1.232	1.246	1.251	1.252	1.252	1.244	1.251	1.252	1.251	1.250	1.250	1.252	1.251	1.250	1.249	1.252	1.252	1.250	1.249	1.246
		+30%	1.214	1.235	1.246	1.251	1.253	1.235	1.247	1.252	1.253	1.252	1.246	1.252	1.253	1.252	1.250	1.251	1.253	1.252	1.250	1.249	1.253	1.252	1.251	1.249	1.246
		-30%	1.196	1.224	1.238	1.246	1.250	1.224	1.240	1.248	1.251	1.251	1.238	1.248	1.251	1.250	1.249	1.246	1.251	1.250	1.249	1.248	1.250	1.251	1.249	1.248	1.247
		-15%	1.204	1.229	1.242	1.248	1.251	1.229	1.244	1.250	1.252	1.251	1.242	1.250	1.252	1.251	1.250	1.248	1.252	1.251	1.250	1.249	1.251	1.252	1.250	1.249	1.247
T_a	0%	W_a 0%	1.210	1.233	1.245	1.250	1.253	1.233	1.246	1.252	1.253	1.252	1.244	1.252	1.253	1.252	1.250	1.250	1.253	1.252	1.250	1.249	1.253	1.252	1.250	1.249	1.246
		+15%	1.216	1.236	1.247	1.252	1.253	1.236	1.248	1.253	1.254	1.253	1.246	1.253	1.254	1.252	1.251	1.252	1.254	1.252	1.251	1.249	1.254	1.253	1.251	1.249	1.246
		+30%	1.220	1.239	1.248	1.253	1.254	1.238	1.249	1.254	1.254	1.253	1.248	1.254	1.254	1.253	1.251	1.253	1.254	1.253	1.251	1.249	1.254	1.253	1.251	1.249	1.245
		-30%	1.202	1.228	1.241	1.248	1.251	1.227	1.243	1.250	1.252	1.251	1.241	1.250	1.252	1.251	1.250	1.248	1.252	1.251	1.250	1.249	1.251	1.251	1.250	1.249	1.247
		-15%	1.209	1.233	1.244	1.250	1.253	1.232	1.246	1.252	1.253	1.252	1.244	1.252	1.253	1.252	1.250	1.250	1.253	1.252	1.250	1.249	1.253	1.252	1.251	1.249	1.247
	+15%	0%	1.215	1.236	1.247	1.252	1.254	1.236	1.248	1.253	1.254	1.253	1.246	1.253	1.254	1.252	1.251	1.252	1.254	1.252	1.251	1.249	1.254	1.253	1.251	1.249	1.246
		+15%	1.220	1.239	1.249	1.253	1.255	1.239	1.250	1.254	1.255	1.253	1.248	1.254	1.254	1.253	1.251	1.253	1.255	1.253	1.251	1.249	1.255	1.254	1.252	1.249	1.246
		+30%	1.225	1.242	1.250	1.254	1.255	1.241	1.251	1.255	1.255	1.254	1.250	1.255	1.255	1.253	1.252	1.254	1.255	1.253	1.252	1.249	1.255	1.254	1.252	1.249	1.245
		-30%	1.206	1.231	1.243	1.249	1.252	1.230	1.245	1.251	1.252	1.252	1.243	1.251	1.253	1.252	1.250	1.249	1.253	1.252	1.250	1.249	1.252	1.252	1.250	1.249	1.247
		-15%	1.214	1.235	1.246	1.252	1.254	1.235	1.248	1.253	1.254	1.253	1.246	1.253	1.254	1.252	1.251	1.251	1.254	1.252	1.251	1.249	1.254	1.253	1.251	1.249	1.246
	+30%	0%	1.219	1.239	1.248	1.253	1.255	1.238	1.250	1.254	1.255	1.254	1.248	1.254	1.255	1.253	1.252	1.253	1.255	1.253	1.251	1.249	1.255	1.254	1.252	1.249	1.246
		+15%	1.224	1.242	1.250	1.254	1.255	1.241	1.251	1.255	1.255	1.254	1.250	1.255	1.255	1.254	1.252	1.254	1.255	1.254	1.252	1.249	1.255	1.254	1.252	1.249	1.245
		+30%	1.229	1.244	1.252	1.255	1.256	1.244	1.253	1.256	1.256	1.255	1.252	1.256	1.256	1.254	1.252	1.255	1.256	1.254	1.252	1.249	1.256	1.255	1.252	1.249	1.245

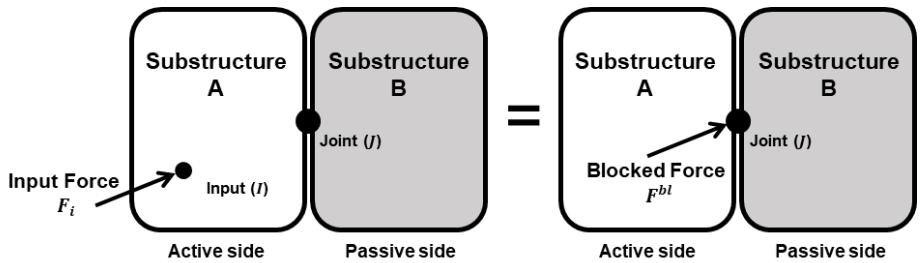

Figure 5.1 Schematic of a combined system with actual input force (left) or virtual blocked force (right)

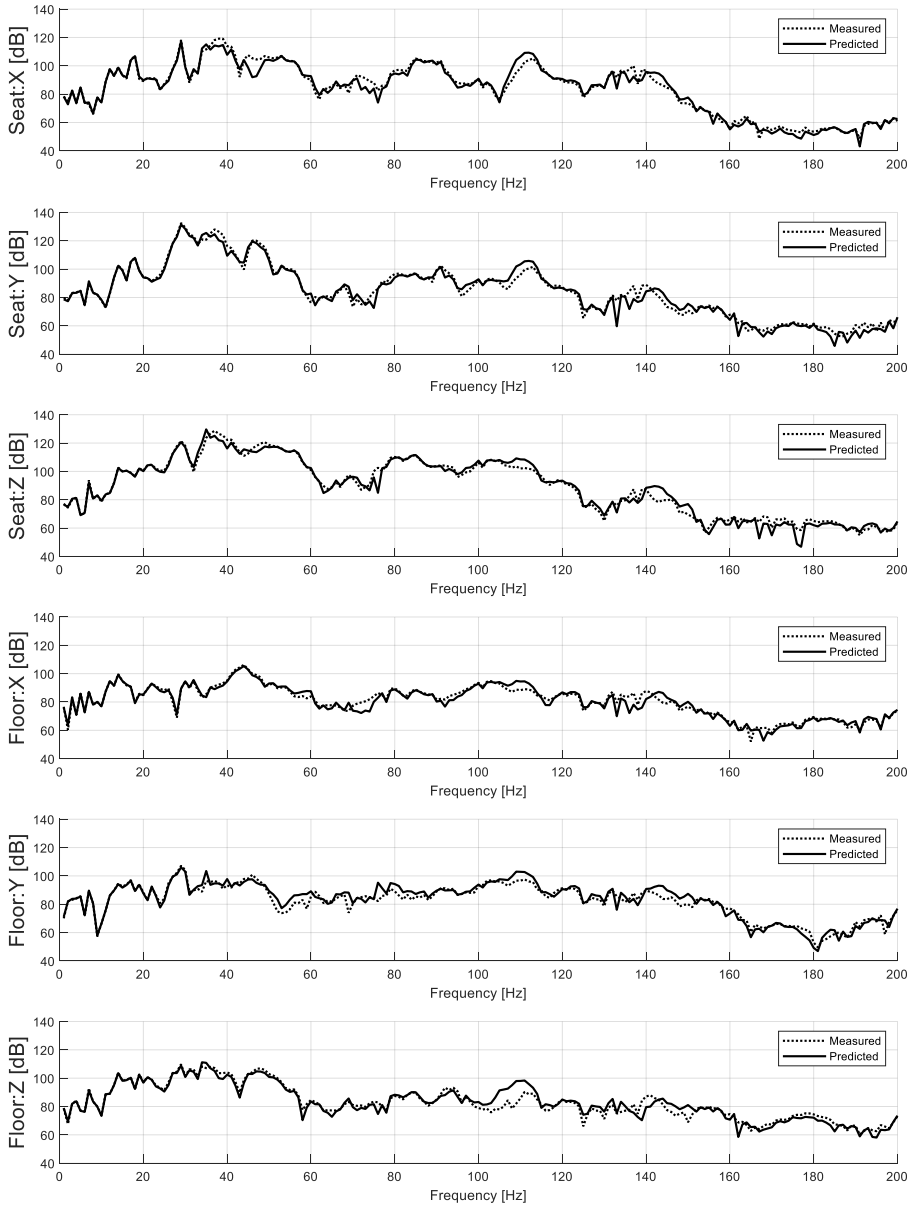

Figure 5.2 Predicted vibratory responses of the tested vehicle subsystem at the output positions

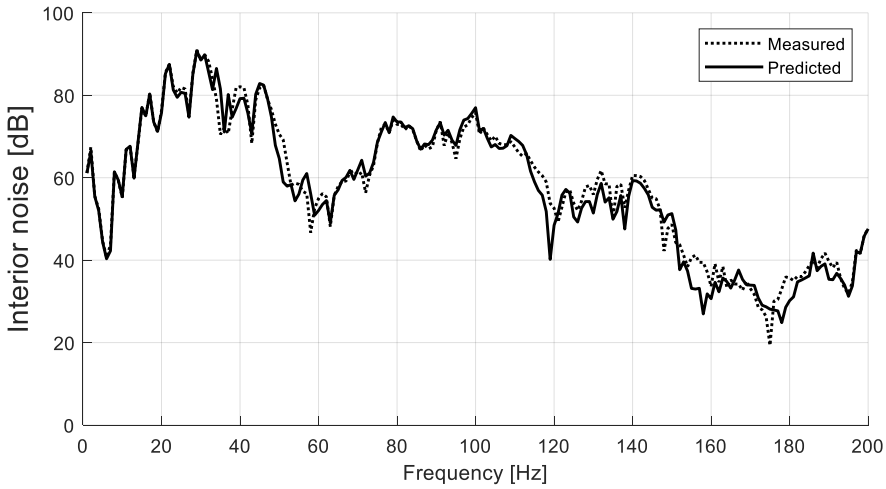

Figure 5.3 Predicted vehicle interior noise of the tested vehicle subsystem at the driver's ear position

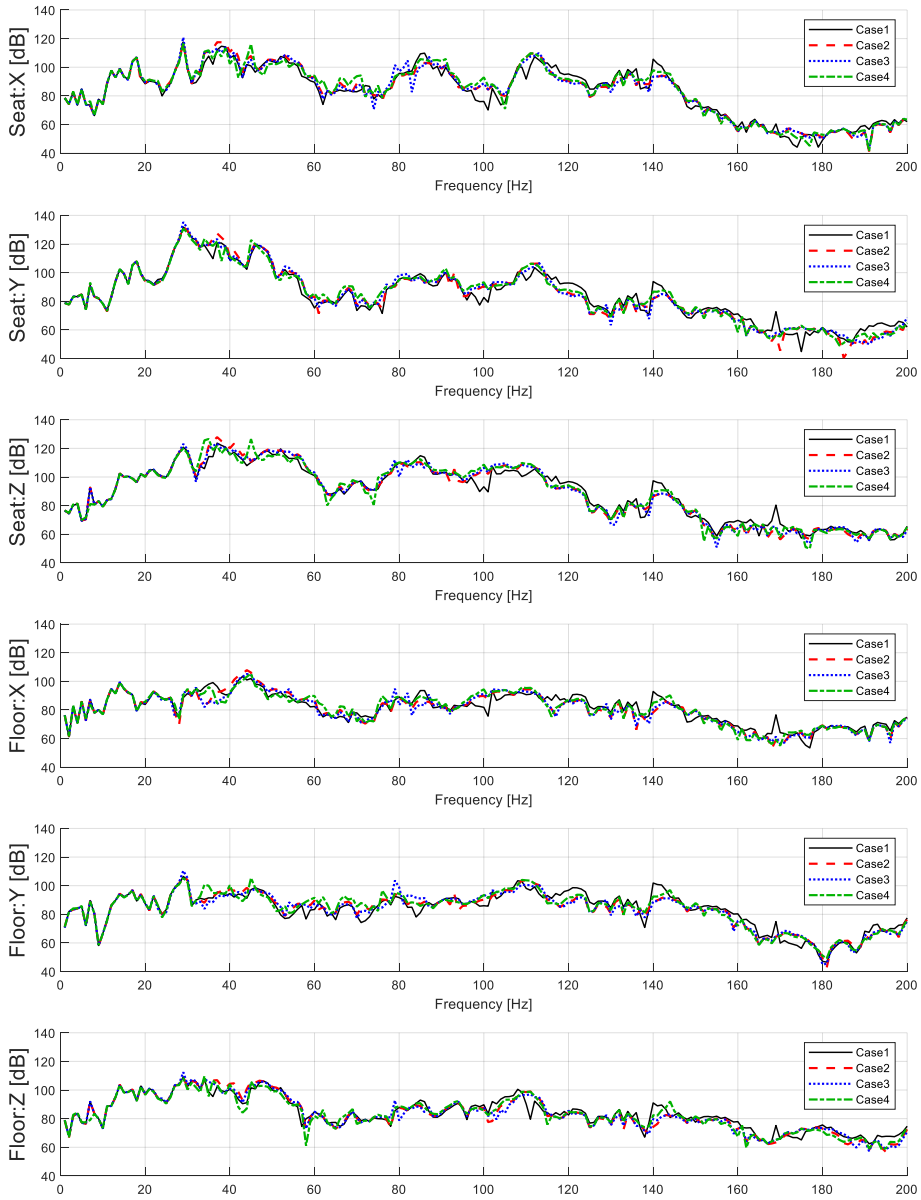

Figure 5.4 Predicted vibratory responses at the output position for the four frame-shaped subcomponents

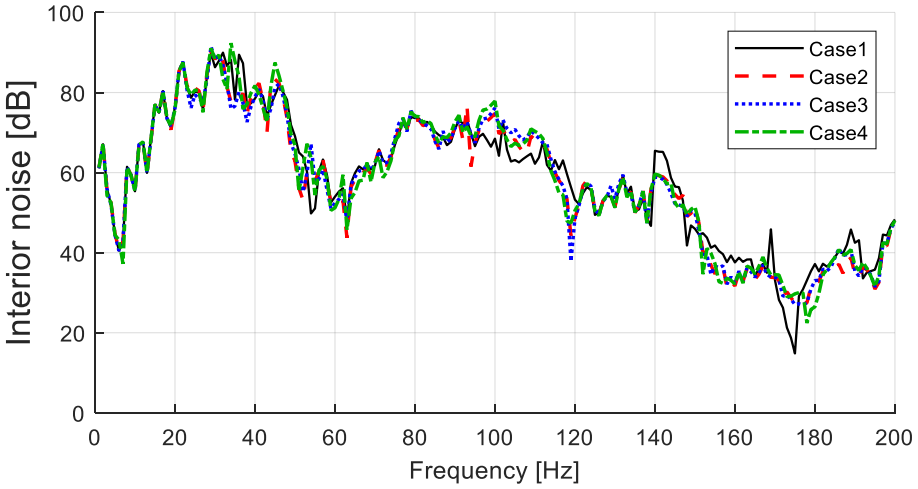

Figure 5.5 Predicted interior noise at the driver's ear position for the four frame-shaped subcomponents

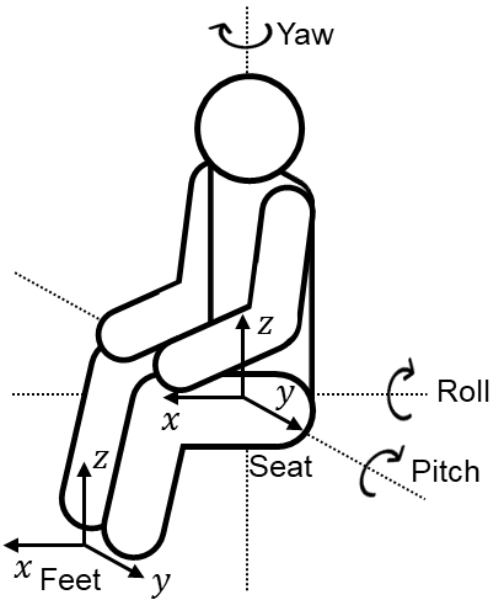

Figure 5.6 Axes of the human body in the seated posture

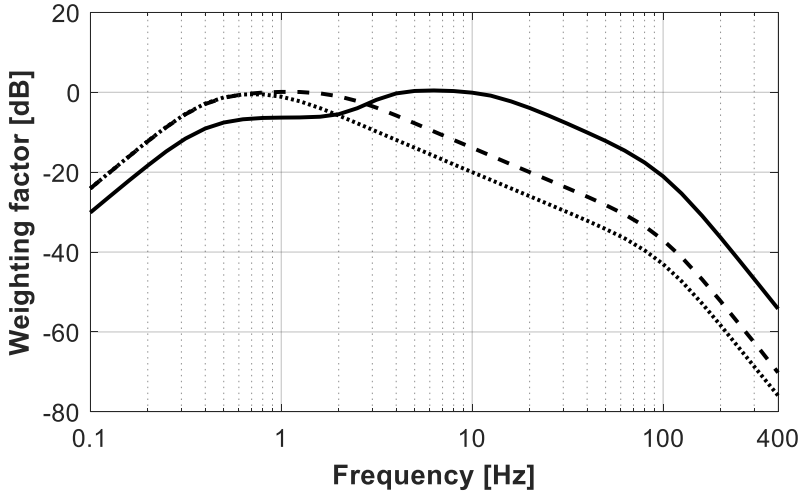

Figure 5.7 Weighting curves for vibration perception in ISO 2631-1; $\mathbf{W_d}$ (dashed line), $\mathbf{W_e}$ (dotted line), $\mathbf{W_k}$ (solid line)

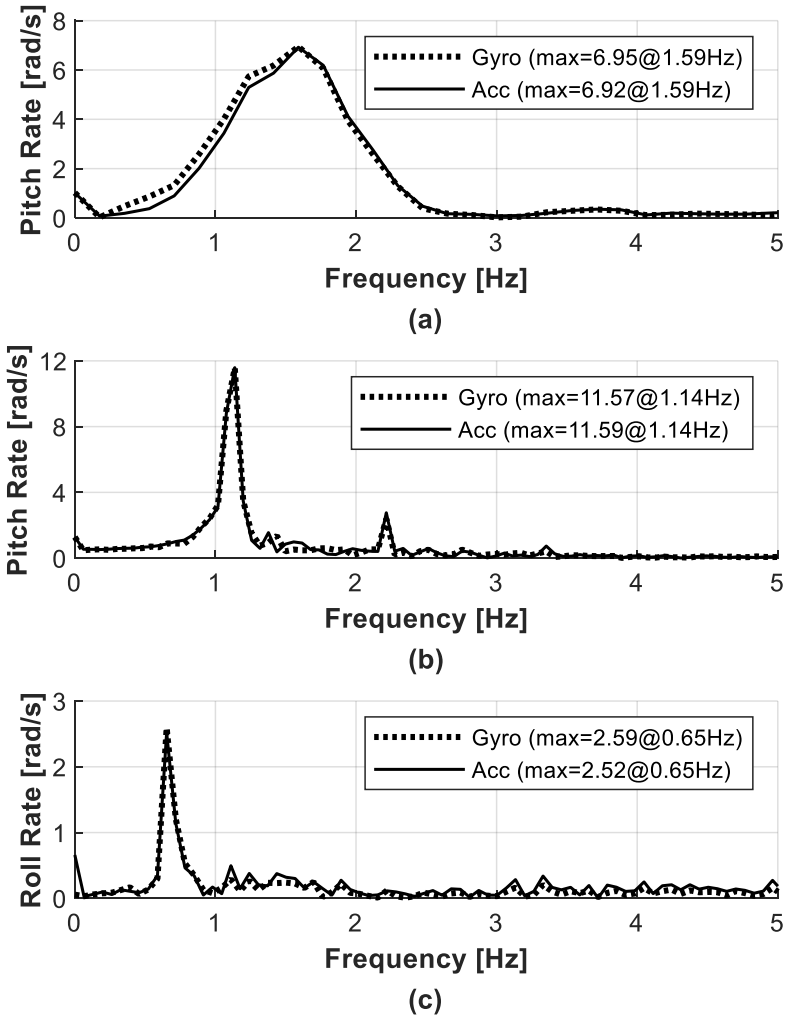

Figure 5.8 Spectral dynamic responses of three axes of rotational motions measured using a gyro-type sensor (dotted line) and four accelerometers (sold line). (a) pitch rate at the bump road, (b) pitch rate at the long-wave road, and (c) roll rate at the twist road

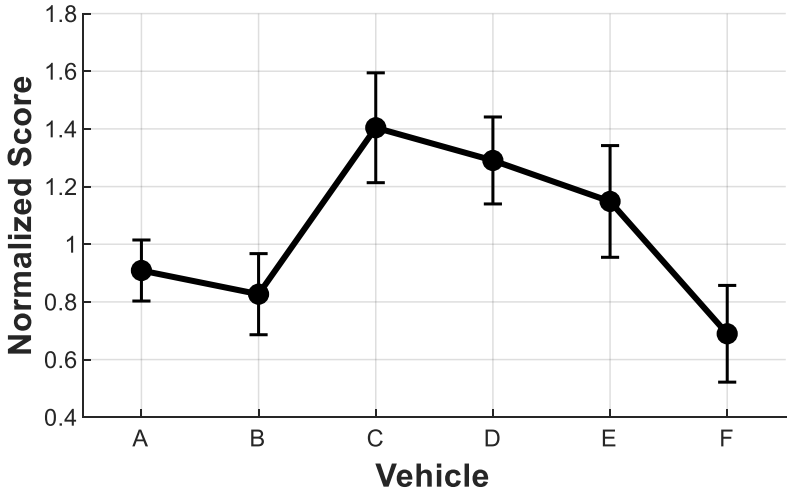

Figure 5.9 Averaged scores of target vehicles for the primary ride test conditions

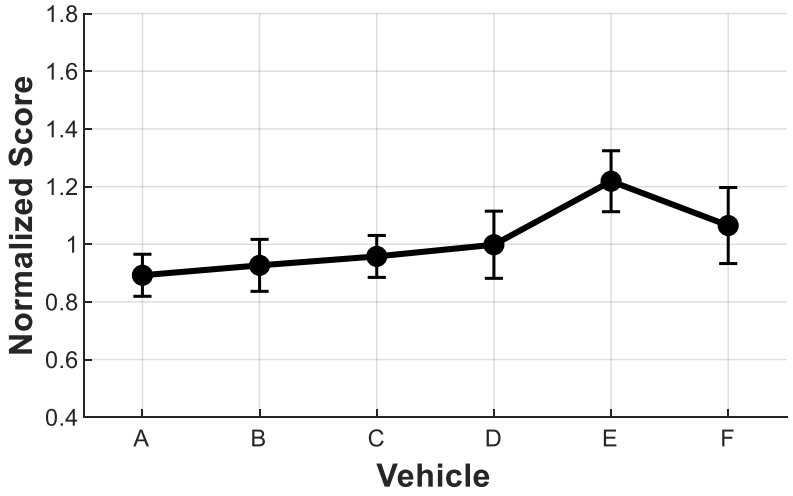

Figure 5.10 Averaged scores of target vehicles for the secondary ride test conditions

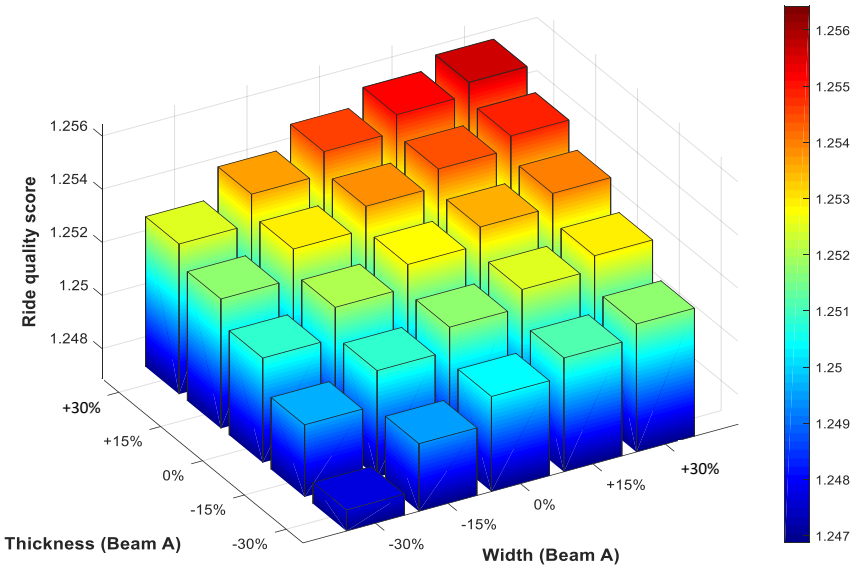

Figure 5.11 Ride quality scores for the changes of the thickness and width of Beam A

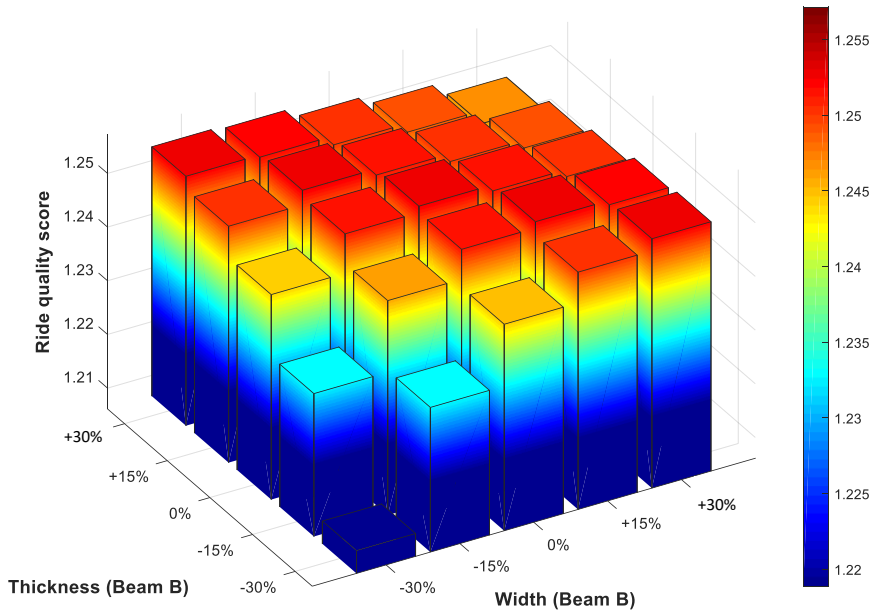

Figure 5.12 Ride quality scores for the changes of the thickness and width of Beam B

CHAPTER 6

CONCLUSION

In this study, a predictive method was proposed to estimate the changes in the transfer characteristics of a complex system due to a modification of a frame-shaped substructure. The purpose of this study is to provide a proactive method predicting the changes in the frequency response function from a minor modification of subcomponents. Because of the phenomenological characteristics of vibration, it is difficult to evaluate the vibration of a machenary system prior to the manufacture and the experimentation of test samples. In order to reduce time and cost in the research process for vibration reduction, several studies on predictive methods have been conducted, but no methodology that is highly accurate enough to be used directly in the actual industry has not been released so far. In accordance with this situation, this study did not aim a perfect prediction of the dynamic behavior of a complex system, but focused on investigating how the transfer characteristics of the initially tested system change according to the changes in specific subsystems.

This study was started with the theoretical analysis of a frame-shaped subcomponent. In chaper 3, three dimensional dynamic behaviors of a rigid frame structure were analyzed based on Euler–Bernoulli and Timoshenko–

Ehrenfest beam theories. The dynamic motions were defined by the equations from the boundary conditions at the each end of the structure and the coupling constraint at the structural joint. The entire set of the equations were united as the form of linear algebraic formulation that are simple to compute and highly scalable in the modification of a substructure.

In chapter 4, the predicted transfer characteristics of the frame substructure and the measured transfer characteristics of the rest of the system were combined using the dynamic substructuring technique. This study confirmed how the transfer characteristics of the full vehicle system changes according to a modification of a frame-shaped subcomponent. In this study, the concept of the joint property was applied to enhance the accuracy of the prediction. The dynamic properties of the subsystem of the vehicle and the joint properties were measured for the initial unchanged system, and the change in dynamic characteristics of the entire system was predicted without additional experiments by applying the theoretically predicted dynamic properties while substituting a specific part to a rigid frame structure.

To utilize the proposed predictive method, two application cases were studied in chapter 5. The dynamic responses were obtained by multiplying the predicted transfer characteristics of the modified system by the blocked force, which is a virtual input force substituting the indefinable input force. For the

testing situation of road driving condition, vibration at the human contact position to the vehicle system and vehicle interior noise were predicted using the predictive dynamic substructuring technique.

Moreover, a quantitative evaluation models for the prediction of changes in perceptual characteristics from the changed vibration. A quantitative evaluation methods to evaluate the characteristics of human perception for the vehicle induced vibration were studied. Subjective evaluation and objective measurement were perforem coincidently during driving test, and the results of two testing procedure were correlated using statistical analyses. The principal component analysis was used to simplify the testing procedure, and multiple linear regression analysis was used to construct the relationship between subjective scores and measured vibrations.

As a verification experiment of these studies were conducted for a vehicle system mentioned in chapter 4.3. The dynamic characteristics of a rigid frame structure which substitutes a frame-shaped subcomponent of the vehicle suspension system were predicted based on the investigation of chapter 3. This predicted result was combined with the measured characteristics of the rest of the subsystem that had been obtained from the original vehicle system. The changes in the transfer characteristics due to the component substitution were predicted well as shown in chapter 4. Finally, the dynamic responses were

predicted for the changes of the characteristics of subcomponent, and the perceived ride quality were calculated from the vibratory responses by applying the secondary RQI model as described in chapter 5. This prediction of dynamic responses and the consequent subject perception were performed for several modifications of the target frame-shaped subcomponent.

As mentioned at the beginning of this chapter, this study aims to predict the changes in the transfer characteristics of the system according to the modification in a specific subsystem. In this study, changes in vibration transfer characteristics were estimated with high accuracy, and it was possible to predict changes in vibration, road-noise and perceptual scores of the modified system. However, this study also has some limitations. This study predicts the result of simple modification of one subcomponent of the entire system, and although the prediction performed in Chapter 4 showed higher accuracy than other studies, an error occurred at 100 to 150 Hz, which is considered an experimental limit. In addition, since it was impossible to analyze the perfect mechanism for the change in transfer characteristics and it must be judged phenomenologically through parametric studies on the predicted results, further research is needed in the future. Inspite of these limitations, it can contribute to the development of the predictive evaluation techniques for the dynamic responses occurring in mechanical systems. Furthermore, by overcoming these limitations, it is

expected that the proactive evaluation method will be further improved by subsequent researches.

REFERENCES

[1] J. S. Tsai and Y. F. Chou, “The identification of dynamic characteristics of a single bolt joint,” J. Sound Vib. 125(3), 487–502 (1988).

[2] B. Jetmundsen, R. Bielawa, and W. Flannelly, “Generalized frequency domain substructure synthesis,” J. Am. Helicopter Soc. 33(1), 55–65 (1988).

[3] D.J. Ewins and P.T. Gleeson, “A method for modal identification of lightly damped structures,” J. Sound Vib. 84(1), 57–79 (1982).

[4] M. Wang, D. Wang, and G. Zheng, “Joint dynamic properties identification with partially measured frequency response function,” Mech. Syst. Signal Process. 27, 499–512 (2012).

[5] M. Mehrpouya, E. Graham, and S.S. Park, “FRF based joint dynamics modeling and identification,” Mech. Syst. Signal Process. 39(1–2), 265–279 (2013).

[6] S. Tol and H.N. Ozgüven, “Dynamic characterization of bolted joints using FRF decoupling and optimization,” Mech. Syst. Signal Process. 54–55, 124–138 (2015).

[7] H. Cao, S. Xi, and W. Cheng, “Model updating of spindle systems based on the identification of joint dynamics,” Shock Vib. 2015, 894307 (2015).

[8] T. Yang, S.-H. Fan, and C.-S. Lin, “Joint stiffness identification using FRF measurements,” Comput. Struct. 81(28–29), 2549–2556 (2003).

[9] J. Zhen, T.C. Lim, and G. Lu, “Determination of system vibratory response characteristics applying a spectral-based inverse sub-

structuring approach. Part I: Analytical formulation," Int. J. Vehicle Noise Vib. 1(1–2), 1–30 (2004).

[10]M.S. Allen, R.L. Mayes, and E.J. Bergman, "Experimental modal substructuring to couple and uncouple substructures with flexible fixtures and multi-point connections," J. Sound Vib. 329(23), 4891–4906 (2010).

[11]A.T. Moorhouse, A.S. Elliott, and T.A. Evans, "In situ measurement of the blocked force of structure-borne sound sources," J. Sound Vib. 325(4–5), 679–685 (2009).

[12]S. W. B. Klaassen, M. V. Van der Seijs, and D. De Klerk, "System equivalent model mixing," Mech. Syst. Signal Process. 105, 90–112 (2018).

[13]M. V. Van der Seijs, "Experimental dynamic substructuring: analysis and design strategies for vehicle development," PhD Thesis, Delft University of Technology, The Netherlands (2016).

[14]M. V. Van der Seijs, E. A. Pasma, D. D. Van den Bosch, et al., "A benchmark structure for validation of experimental substructuring, transfer path analysis and source characterisation techniques," in Dynamics of Coupled Structures, M. S. Allen, R. L. Mayes, and D. J. Rixen (eds), Vol. 4, Springer Nature, London, pp. 295–305 (2017).

[15]Y.J. Kang, J.G. Kim, D.P. Song, et al., "Derivation of road noise improvement factor within a suspension system using the inverse substructuring method," P. I. Mech. Eng. D – J. Aut., vol. 233, no. 14, pp. 3775-3786, (2019).

[16]Y.J. Kang, D.P. Song, and K.D. Ih, "Estimation of body input force transmission change due to parts' modification using the impedance method under rolling excitation," P. I. Mech. Eng. D – J. Aut., vol. 233, no. 2, pp. 363-377, (2019).

[17]D.P. Song, D. Min, Y.J. Kang, et al., "A methodology for evaluating the structure-borne road noise prior to a prototype vehicle using direct force measured on a suspension rig," Noise Control Eng. J., vol. 64, no. 3, pp. 295-304, (2016).

[18]J.G. Kim, K.U. Nam, and Y.J. Kang, "Method to estimate rotational stiffness: trial masses, virtual masses, and virtual springs," J. Sound Vib., vol. 477, p. 115321, (2020).

[19]J.G. Kim, H.S. Park, M.H. Cho, et al., "Accuracy improvement method for dynamic substructuring models in vehicle systems," J. Vib. and Control, vol. 0, no. 0, pp. 1-13, (2020).

[20]C. Chang, "Vibrations of frames with inclined members," J. Sound Vib., vol. 56, no. 2, pp. 201-214, (1978).

[21]C. Kirk and S. Wiedemann, "Natural frequencies and mode shapes of a free–free beam with large end masses," J. Sound Vib., vol. 254, no. 5, pp. 939-949, (2002).

[22]H. Lin and J. Ro, "Vibration analysis of planar serial-frame structures," J. Sound Vib., vol. 262, no. 5, pp. 1113-1131, (2003).

[23]F. Williams, "An algorithm for exact eigenvalue calculations for rotationally periodic structures," Int. J. Numer. Methods Eng., vol. 23, no. 4, pp. 609-622, (1986).

[24]D. Moon and M. Choi, "Vibration analysis for frame structures using transfer of dynamic stiffness coefficient," J. Sound Vib., vol. 234, no. 5, pp. 725-736, (2000).

[25]B. Chouvion, C. Fox, S Mcwilliam and A Popov, "In-plane free vibration analysis of combined ring-beam structural systems by wave propagation," J. Sound Vib., vol. 329, no. 24, pp. 5087-5104, (2010).

[26]C. Mei, "Analysis of in-and out-of plane vibrations in a rectangular frame based on two-and three-dimensional structural models," J. Sound Vib., vol. 440, pp. 412-438, (2019).

[27]T. Ritto, R. Sampaio and R. Aguiar, "Uncertain boundary condition Bayesian identification from experimental data: A case study on a cantilever beam," Mech. Syst. Signal Process., vol. 68, pp. 176-188, (2016).

[28]Y. Ren and C. Beards, “On substructure synthesis with FRF data,” J. Sound Vib. 185 (5), 845-866 (1995).

[29]D. de Klerk, D.J. Rixen and S. Voormeeren, “General framework for dynamic substructuring: history, review and classification of techniques,” AIAA J. 46 (5), 1169-1181 (2008).

[30]M.V. Van der Seijs, D.D. Van den Bosch, D.J. Rixen and D. de Klerk, “An improved methodology for the virtual point transformation of measured frequency response functions in dynamic substructuring,” 4th ECCOMAS Themat. Conf. Comput. Methods Struct. Dyn. Earthq. Eng., No. 4 (2013).

[31]D.D. Van den Bosch, M.V. Van der Seijs and D. de Klerk, “Validation of blocked-force transfer path analysis with compensation for test

bench dynamics," Dynamics of Coupled Structures, Vol. 1: Proc. of the 32nd IMAC, A Conf. Expo. Struct. Dyn., Springer, New York (2014).

[32]J.G. Kim, K.U. Nam and Y.J. Kang, "Evaluation of noise transfer path contributions using virtual springs with infinite stiffness," Appl. Acoust. 178, 107991 (2021).

[33]S. S. Rao, "Vibration of Continuous Systems", 2nd ed., John Wiley & Sons Inc., New Jersey (2019).

[34]G. Cowper, "The shear coefficient in Timoshenko's beam theory," ASME J. Appl. Mech. 33 (2), 335-340 (1966).

[35]A. P. Boresi, R. J. Schmidt, and O. M. Sidebottom, "Advanced Mechanics of Materials", John Wiley & Sons Inc., New York (1985).

[36]S. N. Patnaik, R. M. Coroneos, and D. A. Hopkins, "Compatibility conditions of structural mechanics," Int. J. Numer. Methods Eng. 47 (1-3), 685-704 (2000).

[37]H. Park and Y. J. Kang, "Analysis of three-dimensional dynamic behavior in rigid frame structures," J. Sound Vib., vol. 551, 117601 (2023).

[38]N. H. Baharin and R. A. Rahman, "Effect of accelerometer mass on thin plate vibration," J. Mekanikal. 29 (2), 100-111 (2009).

[39]D. J. Ewins, Modal Testing: Theory, Practice and Application, John Wiley & Sons (2009).

[40]W. Heylen and S. Lammens, "FRAC: A Consistent way of Comparing Frequency Response Functions," Proc. Int. Conf. Identif. Eng. Syst., 48-57 (1996).

[41]Z. Saeed, C. M. Firrone, and T. M. Berruti, “Joint identification through hybrid models improved by correlations,” J. Sound Vib., vol. 494, 115889 (2021).

[42]T. Miwa, “Evaluation methods for vibration effect: Part 1. Measurements of threshold and equal sensation contours of whole body for vertical and horizontal vibrations,” Ind. Health, 5, 183-205 (1967).

[43]M. J. Griffin, “Subjective equivalence of sinusoidal and random whole-body vibration,” J. Acoust. Soc. Am., 60, 1140-1145 (1976).

[44]M. J. Griffin and E. M. Whitham, “Assessing the discomfort of dual-axis whole-body vibration,” J. Sound Vib., 54 (1), 107-116 (1977).

[45]K. C. Parsons and M. J. Griffin, “The effect of the position of the axis of rotation on the discomfort caused by whole-body roll and pitch vibrations of seated persons,” J. Sound Vib., 58 (1), 127-141 (1978).

[46]P. Donat, A. Grosjean, P. Mistrot, et al., “The subjective equivalence of sinusoidal and random whole-body vibration in the sitting position (an experimental study using the ‘floating reference vibration’ method),” Ergonomics, 26 (3), 251-273 (1983).

[47]P. Mistrot, P. Donati, J. Galmiche, et al., “Assessing the discomfort of the whole-body multi-axis vibration: laboratory and field experiments,” Ergonomics 33(12), 1523-1536 (1990).

[48]H. V. C. Howarth and M. J. Griffin, “The frequency dependence of subjective reaction to vertical and horizontal whole-body vibration at low magnitudes,” J. Acoust. Soc. Am. 83, 1406-1413 (1988).

[49]K. C. Parsons and M. J. Griffin, “Whole-body vibration perception thresholds,” J. Sound Vib. 121(2), 237-258 (1988).

[50]ISO, “Mechanical Vibration and Shock- Evaluation of Human Exposure to Whole Body Vibration — Part 1: General requirements,” International Standard ISO 2631-1, 2nd ed. (1997).

[51]M. Morioka and M. J. Griffin, “Difference thresholds for intensity perception of whole-body vertical vibration: Effect of frequency and magnitude,” J. Acoust. Soc. Am. 107, 620-624 (2000).

[52]C. Kaneko, T. Hagiwara and S. Maeda, “Evaluation of whole-body vibration by the category judgment method,” Ind. Health 43(1), 221-232 (2005).

[53]N. J. Mansfield and S. Maeda, “Equal sensation curves for whole-body vibration expressed as a function of driving force,” J. Acoust. Soc. Am. 117(6), 3853-3859 (2005).

[54]H. Nahvi, M. H. Fouladi, M. Jailani, et al., “Evaluation of whole-body vibration and ride comfort in a passenger car,” Int. J. Acoust. Vib. 14(3), 143-149 (2009).

[55]S. Rahmatalla and J. Deshaw, “Predictive discomfort of non-neutral head–neck postures in fore–aft whole-body vibration,” Ergonomics 54(3), 263-272 (2011).

[56]M. S. Kim, K. W. Kim and W. S. Yoo, “Method to objectively evaluate subjective ratings of ride comfort,” Int. J. Automot. Technol. 12, 831-837 (2011).

[57]N. Mansfield and S. Maeda, “Subjective ratings of whole-body vibration for single-and multi-axis motion,” J. Acoust. Soc. Am. 130(6), 3723-3728 (2011).

[58]J. DeShaw and S. Rahmatalla, “Predictive discomfort in single-and combined-axis whole-body vibration considering different seated postures,” Hum. Factors 56(5), 850-863 (2014).

[59]J. T. Song, S. J. Ahn, W. B. Jeong, et al., “Subjective absolute discomfort threshold due to idle vibration in passenger vehicles according to sitting posture,” Int. J. Automot. Technol. 18, 293-300 (2017).

[60]R. Govindan, V. H. Saran, and S. P. Harsha, “Subjective discomfort analysis of human body in semi-supine posture caused by vertical sinusoidal vibration,” Ergonomics 64 (6), 744-754 (2021).

[61]J. Li and Y. Huang, “The effects of the duration on the subjective discomfort of a rigid seat and a cushioned automobile seat,” Int. J. Ind. Ergon. 79, 103007 (2020).

[62]X. Du, C. Sun, Y. Zheng, et al., “Evaluation of vehicle vibration comfort using deep learning,” Measurement 173, 108634 (2021).

[63]P. Múčka, “International Roughness Index specifications around the world,” Road Mater. Pavement Des. 18, 929-965 (2017).

[64]M. Cutini, M. Brambilla, and C. Bisaglia, “Assessment of a ride comfort number for agricultural tractors: A simplified approach,” Biosyst. Eng. 185, 35-44 (2019).

[65]M. Dumitriu and M. C. Leu, “Correlation between ride comfort index and Sperling's index for evaluation ride comfort in railway vehicles,” Appl. Mech. Mater. 880, 201-206 (2018).

[66]G. Mastinu and M. Plöchl, Road and Off-Road Vehicle System Dynamics Handbook, CRC Press (2014).

[67]H. Baruh, Applied Dynamics, CRC Press, Boca Raton (2015).

[68]M. Bennur, D. Hogland, E. Abboud, et al., “Multi-Disciplinary Robust Optimization for Performances of Noise & Vibration and Impact Hardness & Memory Shake,” SAE Technical Paper (2009).

[69]N. Otto, S. Amman, C. Eaton, et al., “Guidelines for jury evaluations of automotive sounds,” SAE Technical Paper 108 (6), 3015-3034 (1999).

[70]M. Kolich and S. M. Taboun, “Ergonomics modelling and evaluation of automobile seat comfort,” Ergonomics, 47 (8), 841-863 (2004).

[71]I. Joliffe and B. Morgan, “Principal component analysis and exploratory factor analysis,” Stat. Methods Med. Res. 1 (1), 69-95 (1992).

[72]D. A. Freedman, “Statistical models: theory and practice,” Cambridge University Press, (2009).

[73]S. S. Stevens and L. E. Marks, “Psychophysics: Introduction to its perceptual, neural, and social prospects,” Routledge, (2017).

[74]H. Park, Y. J. Kang, M. Kim, et al., “Experimental evaluation models of vehicle ride quality for two vibration types: primary ride and secondary ride.” J. Mech. Sci. Technol. 37, 2301-2309 (2023)

[75]R. A. Fisher, “The Design of experiments,” 7th ed., Hafner Press, (1960).

[76]A. P. Field, “Discovering statistics using SPSS : (and sex, drugs and rock 'n' roll),” 3rd Ed., Los Angeles, SAGE Publications, (2009).

[77]S. Sheather, “A Modern Approach to Regression with R,” Springer Science & Business Media, (2009).

국 문 초 록

본 연구에서는 프레임 형태의 서브시스템의 변형에 따른 결합시스템의 진동응답 변화를 추가적인 실험없이 예측하는 방법을 제안한다. 먼저, 이를 위해 결합된 시스템의 동적 응답을 예측하기 위한 단순화한 공식을 사용하여 프레임 구조의 동적 특성을 이론적으로 분석하였다. Euler-Bernoulli 및 Timoshenko-Ehrenfest 보 이론을 기반으로 빔형상 구성 요소의 경계 조건과 시스템의 접합부에서의 경계조건에 따라 동적 거동을 해석하게 된다. 이러한 전체 공식을 선형 대수 형태로 정리함으로써 다양한 형태의 프레임 구조에 대한 해석이 가능하게 되며, 이 때 동적 거동은 특성 행렬과 외력 벡터에서 계산된 계수 벡터로 결정된다. 이렇게 예측된 서브시스템의 동적 특성은 동특성 합성기법을 통해 측정으로 얻은 다른 서브시스템의 동적 특성과 결합하였다. 이 동특성 합성기법을 사용하기 위해 프레임 형태의 서브시스템의 예측된 동특성과 나머지 시스템의 측정된 동특성을 결합하기 위해 접합부 동특성(Joint property)의 개념을 도입하였다. 이 동특성 합성기법은 차량 시스템에 대한 실험을 통해 검증되었다. 차량 현가계 시스템의 프레임 형태 부품 중 하나를 강성 프레임 구조로 변경할 때, 제안된 동특성 합성기법을 통해 완성차 시스템의 전달특성을 예측하였다. 예측한 전달특성과 측정된 전달함수 사이의 높은 유사도를 통해 예측의 정확도를 확인하였다. 또한, 본

연구에서는 제안하는 방법을 활용하기 위한 두 가지 응용 사례를 소개하였다. 하나는 차량 시스템의 동적응답을 예측하는 것이다. 결합시스템의 예측된 전달 특성에 Blocked Force 라고 하는 가상 입력 힘을 곱하여 추가 실험 없이 승객에게 전달되는 소음 및 진동의 변화를 계산하였다. 다른 응용 사례는 인체에 전달되는 진동에 대한 지각적 특성의 예측이다. 승차감 지수라는 이름으로 차량 진동에 대한 주관적 느낌의 정량화 모델을 개발하였다. 주관적으로 평가한 승차감 점수와 측정된 인체에 전달되는 진동과의 관계를 통계적으로 조사함으로써 차량 승차감의 실험적 평가를 수행하였다. 평가를 위한 실험 절차를 단순화하고 승차감 지수 모델의 수식화하기 위해 주성분 분석 및 다중 선형 회귀 분석이 사용되었다. 구성된 모델의 신뢰성은 통계지표의 계산과 추가적인 검증절차를 거쳐 확인되었다. 이러한 일련의 연구를 통해, 차량 시스템의 특정 하위구조의 변형에 따른 완성차 시스템의 전달 특성 변화를 추가적인 실험 없이 예측할 수 있으며, 최종적으로 운전자가 인지하는 동적응답 및 승차감의 변화까지 예측이 가능함을 확인하였다.

주요어 : 전달특성, 빔 진동 이론, 동특성합성기법,
강성 프레임 구조, 승차감
학 번 : 2015-20728